

Quantum control of I₂ in the gas phase and in condensed phase solid Kr matrix

Christopher J. Bardeen, Jianwei Che, Kent R. Wilson, and Vladislav V. Yakovlev
Department of Chemistry and Biochemistry, University of California, San Diego, La Jolla, California 92093-0339

V. A. Apkarian, C. C. Martens, and R. Zadoyan
Department of Chemistry, University of California, Irvine, Irvine, California 92697-2025

Bern Kohler
Department of Chemistry, Ohio State University, Columbus, Ohio 43210

Michael Messina
Department of Chemistry, University of North Carolina, Wilmington, Wilmington, North Carolina 28403-3297

(Received 28 August 1996; accepted 23 January 1997)

We present experimental results and theoretical simulations for an example of quantum control in both gas and condensed phase environments. Specifically, we show that the natural spreading of vibrational wavepackets in anharmonic potentials can be counteracted when the wavepackets are prepared with properly tailored ultrafast light pulses, both for gas phase I₂ and for I₂ embedded in a cold Kr matrix. We use laser induced fluorescence to probe the evolution of the shaped wavepacket. In the gas phase, at 313 K, we show that molecular rotations play an important role in determining the localization of the prepared superposition. In the simulations, the role of rotations is taken into account using both exact quantum dynamics and nearly classical theory. For the condensed phase, since the dimensionality of the system precludes exact quantum simulations, nearly classical theory is used to model the process and to interpret the data. Both numerical simulations and experimental results indicate that a properly tailored ultrafast light field can create a localized vibrational wavepacket which persists significantly longer than that from a general non-optimal ultrafast light field. The results show that, under suitable conditions, quantum control of vibrational motion is indeed possible in condensed media. Such control of vibrational localization may then provide the basis for controlling the outcome of chemical reactions. © 1997 American Institute of Physics. [S0021-9606(97)01217-8]

I. INTRODUCTION

Quantum control, defined here as using light with a tailored electric field, $E(t)$, to optimally manipulate the quantum dynamics of a system, has attracted great interest in the past decade. It has been shown both theoretically and experimentally that the tailoring of, and the interference among, light fields can be used to control wavepacket dynamics and chemical reactions.¹⁻⁵⁵ However, most experimental and theoretical demonstrations to date have been in the gas phase even though most chemical reactions of interest to synthetic chemists occur in condensed media. In this paper (which extends earlier short reports^{24,51}), we study quantum control in both gas and condensed phases, using the focusing of a vibrational wavepacket on the I₂ B state as our test system. We thus provide a demonstration, both experimental and theoretical, that quantum control is indeed possible in condensed phases.

There are two paradigms for quantum control: a dynamic control scheme, due to Tannor and Rice,² which is based on the creation of non-stationary states using ultrafast light pulses; and a static control scheme, due to Brumer and Shapiro,⁴ that uses two or more cw light fields to cause interference between different pathways to a degenerate final

quantum state. Various implementations of the Tannor-Rice scheme to control a chemical reaction have been experimentally realized by several groups.^{45,53} Herek *et al.*⁴⁸ have shown experimentally that a unimolecular reaction, the photodissociation of NaI, with two distinct exit channels, can be controlled by varying the delay time between two femtosecond excitation pulses. As is discussed below, it has been demonstrated that this product branching ratio in NaI photodissociation can also be controlled by varying the pulse chirp.^{25,51} The Brumer-Shapiro scheme has also been realized experimentally, by Kleiman *et al.*^{32,33} who used it to control the photodissociation of CH₃I and the photoionization of H₂S, by Xing *et al.*⁵² who used it to control photoionization of CH₃I, and by Shnitman *et al.*⁵⁵ who used two-photon incoherent interference to control the branching ratio of the photodissociation of Na₂. Melinger *et al.*^{40,41} have shown that intense chirped pulses can be used to transfer population between electronically excited states both efficiently and selectively. Chirped ultrashort pulses can also be used to selectively excite vibrational wavepacket motion on different electronic states.⁵⁶

The control paradigm used in this paper is of the dynamic Tannor-Rice type and uses tailored ultrafast light fields to drive the quantum dynamics of a system to a desired

target at a desired time. The ability to localize wavepackets by using an optimally tailored ultrafast light field has been discussed theoretically¹⁴ and demonstrated experimentally for gas phase I₂.^{16,18} Such wavepacket focusing can be used as an intermediate step leading to control of the products of a chemical reaction by selective bond excitation and bond breaking, and by the modification of the asymptotic product branching ratios through subsequent excitation to higher electronic states. For instance, one could use a chirped pulse to create a vibrational packet localized in internal coordinate space which can then be efficiently pumped by a second pulse to a dissociative state leading to specific products. Recently, we applied this idea of using wavepacket focusing to control a chemical reaction to the control of the Na*/Na branching ratio in the NaI photodissociation using ultrafast light fields tailored by varying their linear chirp.^{25,51} Thus the condensed phase wavepacket localization demonstrated in the present paper opens the way, at least in principle, to similar quantum control of condensed phase reactions.

In previous gas phase experiments, it was shown that a negatively chirped ultrafast light field can be used to focus an I₂ vibrational wavepacket with incoming momentum, while a positively chirped pulse will defocus the wavepacket.^{16,18} This was a compelling result since it showed that two light fields, both essentially identical in their intensity vs. time and intensity vs. frequency profiles and differing only in the time ordering of their frequencies, can lead to very different wavepacket dynamics.

To date most of the experimental work on quantum control has been limited to small molecules in the gas phase. It is therefore important to extend quantum control to molecules in condensed phases, characterized by a very large number of coupled degrees of freedom, as most chemical reactions which chemists would like to control occur in the condensed phase. It is likely not possible to control all degrees of freedom simultaneously. Fortunately, we as chemists, are usually only interested in a small subset of the degrees of freedom. Examples of such subsets are: a reaction coordinate, reactants and products in a solution reaction, local chromophores which are strongly coupled to external driving fields in solids or liquids, and specific bonds in large molecules. It is desirable and reasonable to consider control of only these primary degrees of freedom which are of special interest. In this model study we show that the concept is realistic. Several theoretical approaches based on this reduced treatment have been presented in earlier work.^{13,15,17,22–24,26,46}

In this paper, we present a more complete treatment of chirped pulse excitation of gas phase I₂ vibrational motion. New experimental and theoretical work shows the importance of taking the initial thermal distribution, both rotational and vibrational, into account when doing these experiments.^{25,51} In particular, we find from exact quantum calculations that rotation must be included to match the experiments, particularly at longer times, but that, with this inclusion, the match between exact quantum calculations and experimental results is very close. Furthermore, we find that a nearly classical theory provides a sufficiently good approximation for the gas phase when compared to exact quan-

tum mechanics and experiment that we can have some confidence that it is also appropriate for the condensed phase, where no test against exact quantum dynamics is possible.

The caging process upon dissociative excitation of I₂ in rare gas matrices had already been studied in some detail.^{57–59} Related I₂/rare gas experiments and theory have been carried out in high density rare gas clusters,^{60–64} and related theory in low and high density supercold rare gas solvents.^{15,17,65–67} More recently, we tested the same principles in the case of dissociative excitation of I₂ (A ³Π_{1,u} state) in solid Kr.⁴⁹ The dynamics following the first outward stretch of the molecular bond is highly non-linear in this A state case,⁴⁹ dominated by the over driven guest-host motions. Despite this high non-linearity, some control over the recombinant molecular wavepacket motion could be exercised by using chirped pump pulses. A theoretical analysis of these processes, with particular emphasis on the effects of using chirped pulses in the preparation and interrogation of the wavepacket dynamics has already been given.⁵⁰ The limited experimental data in this study⁴⁹ are in concert with the theory. The A state control effect is small.

A qualitatively different situation is provided in the case of excitation to the B (³Π_{0,u}⁺) state of I₂ in rare gas solids.⁶⁸ Time resolved studies of this system have shown that vibrational populations, prepared with ultrafast pulses, evolve coherently, until they decay in amplitude due to predissociation, on a time scale of 5–10 ps.⁶⁸ The vibrational dynamics of matrix isolated I₂ (B) presents a paradigm of a system weakly coupled to a bath, and as such, it represents a useful prototype to test the controllability of this general class of condensed phase systems by controlling the tailoring of the radiation fields. To control the time evolution of the wavepacket, for example, to localize it at some later time, the pump pulse must be designed so as to counteract not only the anharmonicity of the molecular potential, but also the dissipation and dispersion effects from the coupling of the molecular coordinate to the bath coordinates.^{15,17,26} Clearly, the cryogenic solid host, with its local order and low thermal occupation of modes, represents a bath which highly limits the initial phase space, with only relatively small dynamical fluctuations. Such a bath provides an experimental system where detailed information about the underlying many-body dynamics can be extracted from molecular dynamics simulations and a careful comparison of theory and experiment. These considerations dictate the choice of systems for the present comparative study of coherent control in the gas and condensed phases.

Earlier theoretical predictions had indicated that some degree of quantum control can be achieved in rare gas condensed media.^{15,17,23,24,49} The theory presented here is based on the Liouville space density matrix formalism^{13,15,17,24,69} which can describe thermal or mixed state systems in a unified fashion. The Liouville formalism also allows for a smooth transition from quantum mechanics through semiclassical mechanics to classical mechanics. Using the density matrix formulation, several approximate approaches to condensed phase control problems have been developed which

include Stochastic Bath (SB),^{13,26} semiclassical Gaussian Wave Packet (GWP) dynamics,^{20,23} Time Dependent Hartree (TDH),^{16,22} and Nearly Classical (NC) mechanics.^{15,17,24,25}

To interpret and numerically simulate our experiments, we carry out further development of Nearly Classical (NC) control and detection theory^{19,27} to reproduce the experimental observable, i.e., the LIF signal. This NC theory^{15,17,24,25} is based on the \hbar expansion of the Liouville space Green functions and gives good agreement with the experimental results.

We also extend experimental and theoretical studies of the gas phase control of molecular I₂, concentrating on the effect of initial rotational populations on quantum control. We find from the exact quantum calculations that rotation and rotational-vibrational coupling must be included to match the experiments, particularly at longer times, but that with their inclusion, the match between exact quantum calculations and experimental results is very close. Furthermore, we find that the NC theory provides a sufficiently good approximation for the gas phase when compared to exact quantum mechanics and experiment that we can have some confidence that it is also appropriate for the condensed phase, where no test against exact quantum dynamics is possible.

This paper is organized as follows. In Sec. II we describe the experimental design. In Sec. III we summarize the experimental results for the quantum control of gas phase I₂. In Sec. IV we present gas phase control and detection theory as well as the numerical simulations and comparisons with experimental results for the gas phase I₂ system. Section V presents the experimental results for the condensed phase I₂/Kr system. Section VI presents the Nearly Classical theoretical approach to condensed phase quantum control and detection as well as the numerical simulations and comparisons with the experimental results for the condensed phase I₂/Kr system. In Sec. VII we discuss the results and conclude.

II. EXPERIMENTAL DESIGN

The experimental apparatus used to detect wavepacket focusing in both the gas and condensed phase experiments is similar to that used previously.¹⁸ The I₂ states involved in the experiments are shown in Fig. 1. We detect the motion of the wavepacket on the B state excited by the first (pump) pulse using a second (probe) pulse delayed in time. The probe pulse excites population from the B state to a higher-lying charge transfer state, either the E state (gas phase)⁵⁷⁻⁵⁹ or the f state (condensed phase).⁶⁸ From these higher-lying states in condensed phase media, the population relaxes to the D' state and the LIF signal from the D' → A' transition is detected. This experimental method has been used previously to monitor the dynamics of I₂ in both gas and condensed phases.^{57-59,62,70} The LIF detection wavelengths are 340 nm in the gas phase and 430 nm in the condensed phase and are chosen to maximize the detected signal and minimize leakage from scattered probe radiation. The reason the detection wavelengths are different between the gas and condensed

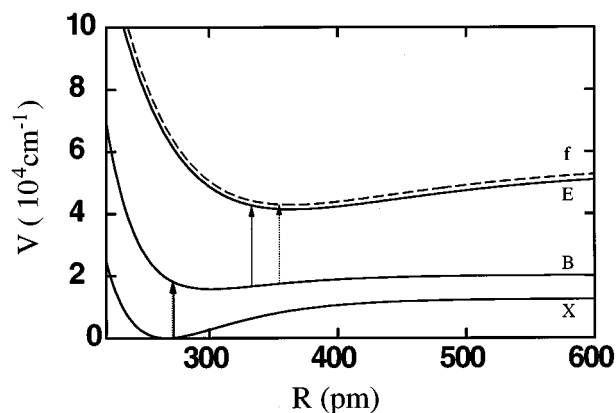


FIG. 1. I₂ potentials as a function of internuclear distance. In the gas phase experiments, the final electronic state is E state, which is shown as a solid line. In the condensed phase experiments, the final electronic state is the solvated f state, which is shown as the dashed line and is lowered by 3900 cm⁻¹ from the gas phase potential. The solid arrows indicate the gas phase pump and probe windows, and the dotted arrows indicate the condensed phase pump and probe windows.

phase experiments is because the D' → A' transition undergoes a large solvatochromatic shift in the Kr matrix.

The experimental apparatus is shown in Fig. 2. The laser system used to generate the ultrafast pump and probe pulses in this experiment has been described before^{18,71,72} and will only be outlined here. The output of a femtosecond Ti:Sapphire oscillator is amplified in a kilohertz regenerative amplifier. The amplified pulse then pumps a two stage Optical Parametric Amplifier (OPA) which is seeded by a continuum generated by a small part of the original pulse.^{71,72} The tunable output of the OPA is then frequency-doubled to yield output pulses in the visible spectral region, which are the pump pulses centered at around 565 nm. The probe pulses at about 395 nm are generated by frequency-doubling the amplified Ti:Sapphire fundamental. Both pulses travel through folded prism compressors (BK7 prisms for the pump and fused silica prisms for the probe) to compensate for the material dispersion resulting from propagation through the non-linear crystals and the optics. The polarization directions

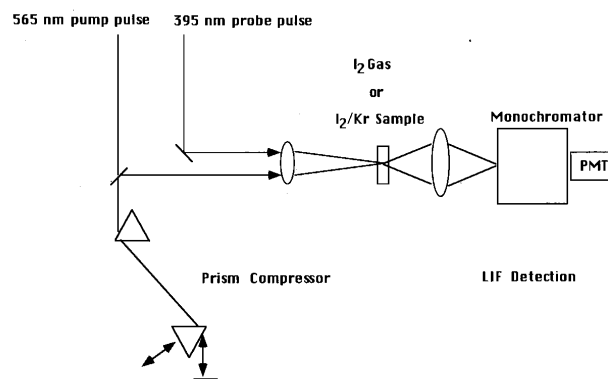


FIG. 2. Schematic of apparatus used for the I₂ control experiments in both the gas and condensed phases.

of the pump and probe are aligned parallel to one another. The final pulse energies at the sample are on the order of 1 microjoule or less.

The pulses, which have been precompensated for the material in the cryostat at windows, cell face, etc., are focused onto the sample by a 20 cm focal length silica lens. In the gas phase experiments, the sample is in a gas bulb at 313 K, and the LIF is detected by a photomultiplier tube (PMT) placed at 90 degrees to the direction of the beams, using a 340 nm interference filter. No other collection optics are used. For the Kr matrix experiments, the sample is held at 15 K in a closed cycle He cryostat and the LIF is collected in the forward direction, along with the scattered laser radiation, and focussed through a 430 nm interference filter and onto the slit of a 0.25-m monochromator. This spectral filtering eliminates most of the scattered probe light. In all experiments the detectors were checked to confirm that the LIF signal was linear with both pump and probe power.

Pulse characterization is a crucial part of these quantum control experiments and we use the Frequency Resolved Optical Gating (FROG) technique for this purpose.^{73,74} This method retrieves, using a numerical algorithm, the electric field, $E(t)$, of the light pulse from a two dimensional experimental measurement of the pulses in frequency and time. The fields, $E(t)$, generated from the FROG data can then be compared to other measures of pulse characteristics, such as the power spectrum or intensity autocorrelation, in order to gauge the reliability of the FROG technique. The consistency among these measurements depends on several factors, including the signal-to-noise ratio and the bandwidth of the pulse, but in general is good. The measured full widths at half maximum (FWHM) of the intensity autocorrelations and those calculated from FROG-derived electric fields agree to within 10 percent at all chirps, with the best agreement obtained when the pulses are close to the transform limit. A comparison is shown in Fig. 3 of the FROG-generated power spectra with the experimentally measured power spectra of the pulses used in the gas phase experiments shown in Fig. 4. The left hand panels of Fig. 3 show the comparison of the pump pulse spectrum (for a representative set of pump pulses) as measured directly (solid line) and as derived from the FROG data (dotted line). As can be seen in Fig. 3, the spectra agree reasonably, although not perfectly. The most important point is that the FROG method provides us with reliable, semi-quantitative, characterizations of the pump and probe $E(t)$ fields used in these experiments, which we then employ in our theoretical simulations. The FROG measurements are done before and after the experiment in order to guard against the possibility of changes in spectrum or phase structure due to drift in the OPA or regenerative amplifier.

Also shown in Fig. 3 are the Wigner transforms of the electric fields generated from the experimental FROG measurements. The Wigner transform maps the field $E(t)$ into a two-dimensional representation in time and frequency, giving a visual image of the tailoring of the pulse. The Wigner transform gives the intensity vs. time of the pump field as the projection onto the time axis, and the intensity vs. frequency (spectral density) of the pump field as the projection onto the

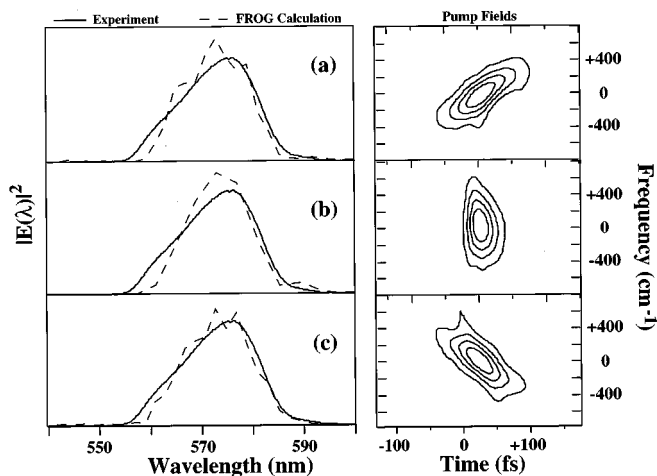


FIG. 3. The left hand panels show the comparison of the experimentally measured (solid line) and FROG-derived (dotted line) spectra for a positively chirped (panel a), transform limited (panel b), and a negatively chirped (panel c) pump pulse. The right hand panels show the FROG-derived Wigner transforms of these pulses. (An overall carrier frequency of 572 nm and a central time have been removed from the Wigners, and all Wigners have been smoothed for clarity).

frequency axis. In the right hand panels of Fig. 3, we show the FROG-derived Wigner transforms for a positively chirped pulse (panel a), transform limited pulse (panel b), and negatively chirped pulse (panel c). For example, a positively chirped pulse will have its lower frequency components arriving earlier in time and its Wigner transform will be a set of contours with an overall positive slope, as shown in panel (a) of Fig. 3. A pulse with a negative linear chirp

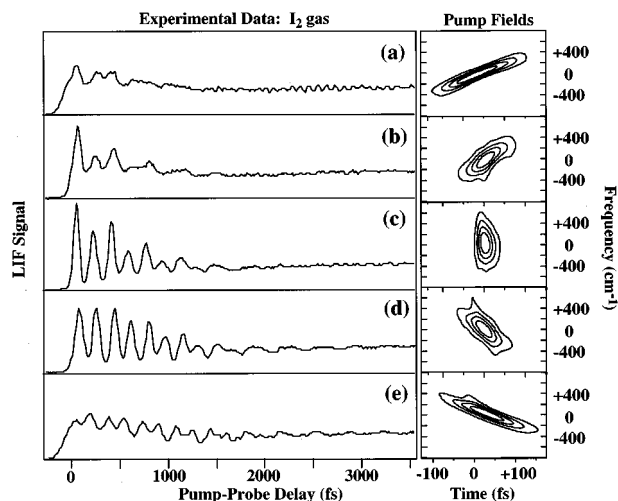


FIG. 4. Summary of the experimental measurements for 313 K gas phase I₂. The left hand panel of Fig. 4 shows the collected LIF signals for excitation with pump pulses that have positive chirps (panels a and b), a transform limited pump pulse (panel c), and pump pulses that have negative chirps (panels d and e). The right hand panel of Fig. 4 shows the FROG-derived Wigner transforms of these pump fields. (An overall carrier frequency of 572 nm and a central time has been removed from the fields in presenting these figures.)

will have a set of contours with an overall negative slope, as shown in panel (c) of Fig. 3, while a transform-limited pump pulse will have all the frequency components arriving simultaneously, as shown in panel (b). In general, we can also write an electric field in frequency space as follows,

$$\tilde{E}(\omega) = A(\omega)e^{i\varphi(\omega)}, \quad (1)$$

where $A(\omega)$ is the slowly varying envelope function, and $\varphi(\omega)$ is the frequency dependent phase of the electric field. $\tilde{E}(\omega)$ can be obtained through a Fourier transform of its time domain representation, $E(t)$. Quantitatively, we define the frequency domain linear chirp²⁹ of an electric field, c' , as the second order coefficient in the Taylor expansion of its phase, $\varphi(\omega)$, in frequency domain around its center frequency ω_0 ,

$$c' = \frac{1}{2} \left. \frac{\partial^2 \varphi}{\partial \omega^2} \right|_{\omega = \omega_0}. \quad (2)$$

Roughly speaking, on the Wigner contour plot, there is a center time at each frequency and these centers form a principle axis of the contour plot as a function of frequency. The slope which gives the linear frequency chirp is then defined as the tangent formed by the frequency axis and this principle axis.²⁹ Specifically, the field in panel (a) of Fig. 4 has larger positive chirp than the one in panel (b).

III. EXPERIMENTAL RESULTS: GAS PHASE

The goal of the experiments described in this section is to more clearly demonstrate the effect of the tailoring of the pump pulse on the vibrational dynamics of the I₂ molecule in the gas phase, and to test the accuracy of the NC approximation (which we will apply to the I₂/Kr system) on a system in which we can carry out the exact quantum mechanics, and then to test both exact quantum dynamics and the NC approximation against gas phase experiment. We use two different pump pulses, both of which have essentially the same intensity vs. time, and intensity vs. frequency profiles, thus differing only in the time ordering of their frequencies. We show theoretically and experimentally that varying the frequency-temporal ordering leads to different vibrational dynamics of the I₂ molecule, the positive chirp delocalizing and the negative chirp localizing the wavepacket. The pump pulse creates the wavepacket on the B state (see Fig. 1), and the dynamics of the I₂ vibrational motion are then monitored via fluorescence induced by the probe pulse, which is delayed relative to the pump pulse. The probe pulse opens a small window in coordinate space, through which the I₂ vibrational wavepacket on the B state passes as it is further excited to the E state. In general, the more localized the peaks in the collected LIF signal vs. delay time, the more localized the vibrational I₂ wavepacket on the B state.^{19,27}

Figure 4 summarizes the experimental results for gas phase I₂. The left hand panel shows the collected LIF signals for excitation with pump pulses that have positive chirps (panels a and b), a transform limited pump pulse (panel c), and pump pulses that have negative chirps (panels d and e). All the pump pulses have essentially the same frequency spectrum. The right hand panel of Fig. 4 shows the FROG-

derived Wigner transforms of these pump fields. The probe pulse is an approximately transform limited ultrafast pulse of 50 fs FWHM with a carrier frequency of 390 nm. This probe pulse opens a window centered at an internuclear distance of 325 pm on the B state potential energy surface (see Fig. 1). Every time the I₂ vibrational wave packet crosses this window, which it does twice per total vibrational cycle, it will be further excited to the probe state, thus giving two LIF peaks per vibrational period. The LIF signal that corresponds to excitation with a positively chirped pump pulse (panel b) clearly shows less vibrational localization which dies out faster in time than the LIF signal that corresponds to excitation with the corresponding negatively chirped pump pulse (panel d). Thus the I₂ vibrational wavepacket initiated by the negatively chirped pump pulse retains its vibrational localization longer than that of the wavepacket initiated with the positively chirped pump pulse. Furthermore, the second oscillation in panel (d) is larger than that of the signal resulting from the transform limited pulse in panel (c). The height of the peak is directly related to the amount of population in the probe window, and the higher peak is the result of the focused wavepacket's having more population in that region of the PES at the appropriate delay.¹⁸ The right hand panel of Fig. 4 clearly demonstrates that the pump fields that give rise to the LIF signals in panels (b) and (d) are a nearly matched pair of chirped pump fields in the sense that they have similar intensity vs time, and intensity vs frequency profiles and differ substantially only in their frequency vs time correlations. The figure also demonstrates that these two pump fields have mainly a linear chirp and only a smaller component of higher order chirp. The LIF signals in panels (a) and (e) also result from a matched pair of chirped pump fields. Again the LIF signal that is collected from the negatively chirped pump pulse (panel e) shows more structure than that of the LIF signal due to the positively chirped pump pulse (panel a). The small oscillations in the strongly positively chirped excitation data (panel a) at about 2.5 ps are reproducible and may result from a wavepacket that has split into several smaller ones. Thus there is an overall trend that a negatively chirped pump pulse leads to a more localized I₂ vibrational wavepacket in the gas phase than that of the equally and oppositely chirped positive pump field. Further the LIF signal in panel (d) shows more structure than the LIF signal in panel (e). The LIF signals in both of these panels arise from negatively chirped pump fields, and this shows that the degree of wavepacket focusing induced by a negatively chirped pump field is a function of the chirp of the pulse, i.e. some negatively chirped pump fields are better than others for inducing vibrational localization by causing wavepacket focusing.

IV. THEORY: GAS PHASE

A. Brief review of quantum control theory: Weak response regime

In this section, we briefly review the theoretical basis for our analysis of these control experiments,^{13,17} using the density matrix language of Liouville space.⁶⁹ The density matrix

formulation has the advantage over the Schrödinger formulation that it can more directly deal with thermal systems and mixed states, and that it allows for a smoother transition among quantum, semiclassical, and classical mechanics. This latter advantage becomes particularly important when we go beyond simple gas phase systems and consider condensed phases. The system evolution is described by the system density matrix, $\rho(t)$, which obeys the quantum Liouville equation,⁶⁹

$$\frac{d\rho}{dt} = \frac{1}{i\hbar}[H, \rho], \quad (3)$$

where H is the system Hamiltonian. For a two electronic level system which is coupled to an external electric field, H has the following form,

$$H = |g\rangle H_g \langle g| + |e\rangle (H_e + \hbar\omega) \langle e| + \vec{D} \cdot \vec{\epsilon}(t), \quad (4)$$

where \vec{D} is the transition dipole operator, defined as,

$$\vec{D} = |e\rangle \vec{\mu}_{eg} \langle g| + |g\rangle \vec{\mu}_{ge} \langle e|. \quad (5)$$

In the weak response limit, the key quantity for calculating both the optimal control field and the spectroscopic response of the system to that field is the material response function. After excitation from the ground electronic state $|g\rangle$ to the excited state $|e\rangle$, this material response function can be written as,¹³

$$M(t_1, t_2) = \text{Tr}[\mathcal{S}_{ee}(t_1) \mathcal{D}_{ee, eg} \mathcal{S}_{eg}(t_2) \mathcal{D}_{eg, gg} \rho_g], \quad (6)$$

where $\mathcal{S}_{ee}, \mathcal{S}_{eg}$ are the excited state and transition Green functions, respectively. $\mathcal{D}_{\mu\nu, \mu'\nu'}$ is the transition dipole matrix operator.¹³ For the calculation of the LIF signal, this function is the non-stationary excited state population that gives rise to the transient absorption to the second excited state. For the quantum control calculation, our objective is to find the optimal electric field that will drive the system dynamics to a desired target state at a particular target time. The measure of quantum control for this system is given by the overlap at the target time, t_f , between the target state and the system density matrix,

$$A(t_f) = \text{Tr}[A\rho(t_f)], \quad (7)$$

where A is our target operator. The target operator A is an operator that projects upon a desired target, which can be any function of quantum observables. In the present work, we choose the target operator A that projects onto a minimum uncertainty wavepacket, and this result is termed wavepacket ‘‘focusing.’’ The above overlap can be maximized subject to various constraints,²⁸ but here we choose a single constraint, the total incident electric field energy. For the weak response regime this choice leads to a simple eigenequation, the eigenfunction of which, corresponding to the largest eigenvalue, is the globally optimal control field.¹³ In this work we will only consider the weak response limit, keeping in mind that the strong response problem can also be solved, by iterative techniques.²¹ To maximize the overlap $A(t_f)$ in Eq. 7,

we employ functional variation of the electric field subject to the constraint of constant field energy, to get the following eigenequation,¹³

$$\int_{t_0}^{t_f} M^s(\tau, \tau') E(\tau') d\tau' = \lambda E(\tau), \quad (8)$$

where $M^s(\tau, \tau')$ is the symmetrized material response function,¹³

$$M^s(\tau, \tau') = [M^s(\tau', \tau)]^* \equiv M(t_f - \tau, \tau - \tau'), \quad \tau \geq \tau'. \quad (9)$$

In Eq. 8, $M^s(\tau, \tau')$ is field-independent in the weak response regime, and λ measures the yield, thus, the electric field corresponding to the largest eigenvalue λ is the globally optimal field in the weak response regime. Once we know how the system evolves independently of the the driving field, $\epsilon(t)$, we can compute the optimal field.¹³

The quantum control theory presented in this and in previous papers can thus be used to compute both the optimal control field and the spectroscopic response induced by that field. Previous theoretical work¹⁴ has concentrated on achieving the target of a localized wavepacket after reflection from the outer turning point, i.e., a molecular reflectron. These earlier calculations have shown that an ultrashort pulse with negative linear chirp is ideal for producing such a wavepacket. Since earlier work has dealt with the theoretical calculation and achievement of such optimal light fields, in this paper we emphasize the practical calculation of the spectroscopic signatures of control using such fields. We concentrate on the experimental creation and use of chirped pulses to demonstrate and characterize the phenomenon of focusing.

B. Exact quantum gas phase control theory

In earlier theoretical and experimental papers, it was shown that gas phase I₂ vibrational wavepackets can be controlled via tailored ultrafast light pulses.¹⁸ Here we extend this work and show that a one dimensional molecular model considering only vibrational dynamics cannot reproduce the longer time behavior of the LIF signals, because rotations start to play an important role after ~ 1 picosecond at room temperature.^{10,11,75,76} One rotational effect, the evolution of the angular distribution of the excited sample, can be eliminated from the LIF signal by aligning the polarization axes of pump and probe beams at the ‘‘magic angle.’’⁷⁷ However, the second rotational effect, the rotational-vibrational coupling, also plays an important role, producing a dispersion in evolution for each set of wavepackets belonging to a single vibrational state but having different total angular momentum. Therefore, it is important to investigate how well we can control the coherent vibrational motion under such conditions. The initial density matrix, including rotational degrees of freedom, can be written as,

$$\rho_g(t) = \sum_{v,J=0}^{\infty} \sum_{M=-J}^J e^{-\beta E_{v,J}^g} \rho_{v,J,M}^g(t), \quad (10)$$

where v, J, M are the vibrational, total angular momentum and magnetic quantum numbers, respectively, g stands for the electronic ground state, $E_{v,J}^g$ is the energy of this v, J rovibrational quantum state in the electronic ground state. We neglect the contributions of electronic orbital and nuclear and electronic spin angular momenta to the total angular momentum, as well as spin-orbital coupling in the calculations but must keep track of the electronic and spin momenta and the spin-orbital coupling in labeling the electronic states, so that for the I₂ molecule with heavy atoms we are led correctly to the strong spin-orbit coupling case, and Hund's case (c) in particular. For Hund's case (c), the "good" electronic quantum number is Ω so that, for example, the ${}^3\Pi_{0_u} \leftarrow {}^1\Sigma_{0^+}$ initial transition is parallel. We assume that the transition from the B state to the probe state is also parallel. Furthermore, the energy of a quantum state does not depend on magnetic quantum number M .

In general, the nuclear density matrix for each quantum state can be written as,

$$\rho_{v,J,M}(t) = |v, J, M; t\rangle \langle v, J, M; t|. \quad (11)$$

Following the above equations, we can evaluate the density matrix by working in Hilbert space. The total wavefunction within an electronic state can be factorized as

$$\psi_{J,M}(R, \theta, \phi, t) = \frac{u_J(R, t)}{R} Y_J^M(\theta, \phi). \quad (12)$$

In Eq. 12, the Y_J^M are the spherical harmonics, R is the internuclear distance coordinate, and θ and ϕ are coordinates in a spherical polar coordinate system. Invoking the Rotating Wave Approximation (RWA), assuming a parallel transition, and using first order perturbation theory with respect to the external field, we have,

$$u_{J-1,M}^e(t) = -\frac{i}{\hbar} \int_0^t dt' e^{-\frac{i}{\hbar} h_e^{J-1}(t-t')} D_{eg} E(t') \times \left[\frac{(J-M)(J+M)}{(2J-1)(2J+1)} \right]^{1/2} u_J^{g_0}(t'), \quad (13)$$

$$u_{J+1,M}^e(t) = -\frac{i}{\hbar} \int_0^t dt' e^{-\frac{i}{\hbar} h_e^{J+1}(t-t')} D_{eg} E(t') \times \left[\frac{(J-M+1)(J+M+1)}{(2J+1)(2J+3)} \right]^{1/2} u_J^{g_0}(t'), \quad (14)$$

where $u_J^{g_0}(t)$ is the ground state wavefunction propagated under the unperturbed radial Hamiltonian h_g^J . In the above, D_{eg} and $E(t)$ are the magnitudes of dipole transition moment and of the pump laser field, respectively. Note that these quantities are treated here as scalars. The superscript J indicates the initial state total angular quantum number, and

$$h_g^J = -\frac{\hbar^2}{2\mu} \frac{\partial^2}{\partial R^2} + V_g(R) + \frac{J(J+1)\hbar^2}{2\mu R^2},$$

$$h_e^J = -\frac{\hbar^2}{2\mu} \frac{\partial^2}{\partial R^2} + V_e(R) + \frac{J(J+1)\hbar^2}{2\mu R^2}. \quad (15)$$

As we will see below, the final angular momentum dependent centrifugal potential terms in these Hamiltonians play an important role in the vibrational wavepacket delocalization. In Eqs. 13 and 14, $E(t)$ is obtained by invoking the RWA,

$$\epsilon(t) = E(t) e^{-i\Omega_{eg}t} + E^*(t) e^{i\Omega_{eg}t}, \quad (16)$$

where Ω_{eg} is the overall carrier frequency of the pump field. Once we have u_J^e , we can then further calculate the population on the excited state reached by the addition of the probe pulse. The sum of all the populations on the final state, each initiating from different ground states $|v, J, M\rangle$, is proportional to the experimentally observed LIF signal.

C. Nearly classical (NC) control theory

For a simple gas phase system such as I₂, the procedure of Boltzmann averaging over initial rovibrational states, although tedious, can be carried out exactly, to any desired degree of accuracy. However, in a condensed phase system consisting of $\sim 10^{23}$ degrees of freedom, it is impossible to perform an exact quantum dynamics calculation. Therefore, we would like an efficient and sufficiently accurate approximation to the exact quantum dynamics. Recently Stochastic Bath (SB),^{13,26} Nearly Classical (NC),^{15,17,24,25} semiclassical Gaussian Wave Packet (GWP),^{20,23} and Time Dependent Hartree (TDH)^{16,22} methods to calculate the optimal fields in the weak response regime for multidimensional systems have been formulated and numerically tested. In what follows, we will review the NC approximation, based on the expansion in \hbar of the exact quantum Green functions, \mathcal{S}_{ee} and \mathcal{S}_{eg} . Classical dynamics has the great advantage of being able to handle large thermal systems (rotation and rotation-vibration coupling are included automatically with no extra work), and it has been applied successfully to problems of this type.^{15,17,57-59} (As we emphasized above, the density matrix formalism allows a smooth transition between quantum mechanics and classical mechanics.) The density matrix evolution on the electronic excited state under perturbation theory is,⁶⁹

$$\rho_e(t) = \left(\frac{i}{\hbar}\right)^2 \int_0^\infty \int_0^\infty dt_2 dt_1 E^*(t-t_2) E(t-t_2-t_1) \times \rho_e^0(t_2, t_1) + \text{h.c.}, \quad (17)$$

where we define $\rho_e^0(t_2, t_1)$ as a bare density matrix since it is physically obtained from the density matrix created by a pair of separated delta pulses,²³

$$\rho_e^0(t_2, t_1) = (i/\hbar)^2 \mathcal{S}_{ee}(t_2) \mathcal{S}_{ee,eg} \mathcal{S}_{eg}(t_1) \mathcal{S}_{eg,gg} \rho_g(-\infty). \quad (18)$$

With an analogy to the density matrix formalism, we work in the phase space of classical trajectories. The ground state density matrix $\rho_g(-\infty)$ can be chosen many different ways and we choose it to be from a classical distribution with quantum correction by means of an artificial temperature,⁷⁸

$$T' = \frac{\hbar \omega}{2k_B} \coth\left(\frac{\hbar \omega}{2k_B T}\right), \quad (19)$$

where T is the real system temperature, and ω in our case is the vibrational frequency of the ground state diatomic. The distribution generated from this procedure is the exact quantum thermal Wigner distribution for a harmonic system, but is only approximate if the system is anharmonic.

The main challenge to computing the exact quantum dynamics for a condensed phase system is that we cannot calculate the Green functions involved in the time evolution of $\rho_e^0(t_2, t_1)$. However, the two Green functions in Eq. 6 can be approximately evaluated from an analogy to classical mechanics, and the Franck vertical transition approximation. First, let us consider $\mathcal{S}_{eg}(t)$, which is defined in terms of an arbitrary operator O as

$$\mathcal{S}_{eg}(t)O \equiv e^{-iH_e t/\hbar} O e^{iH_g t/\hbar}. \quad (20)$$

In classical mechanics there is no quantity analogous to $\mathcal{S}_{eg}(t)$, but we can invoke the vertical transition approximation which is generally good for ultrafast excitation fields. Thus, we can approximate this transition Green function as,^{15,17}

$$\mathcal{S}_{eg}(t) \approx e^{-iU_{eg}t}, \quad (21)$$

where U_{eg} is defined as $U_{eg} \equiv (H_e - H_g)/\hbar$. This equation can be obtained by expanding G_{eg} in a power series in \hbar and keeping only the lowest order term. It is consistent with the static dephasing limit and is equivalent to the truncation of the quantum commutator. In other words, the quantum corrections, which are due to the commutation relation and appear in higher order terms of the expansion, are neglected in the present level of approximation. The same approximation is also used to derive the next equation. The second Green function, $\mathcal{S}_{ee}(t)$, has a simple classical mechanical analog, and we can approximate it as,^{15,17}

$$\mathcal{S}_{ee}(t)(\mathbf{p}, \mathbf{q}, t; \mathbf{p}_0, \mathbf{q}_0) = \delta[\mathbf{p} - \mathbf{p}_e(t)]_0 \delta[\mathbf{q} - \mathbf{q}_e(t)]_0, \quad (22)$$

where $(\mathbf{p}_e(t), \mathbf{q}_e(t))_0$ is the phase space classical trajectory on the excited state propagated from the initial multidimensional phase space point $(\mathbf{p}_0, \mathbf{q}_0)$. These two approximations can be obtained formally by an expansion of the Green functions in a power series of \hbar , the NC Green functions being the leading terms.^{15,17} The NC approximant to \mathcal{S}_{ee} is independent of \hbar , (since \mathcal{S}_{ee} has a classical mechanical analog), and for \mathcal{S}_{eg} , which has no classical analog, the leading term is proportional to \hbar .

Substituting Eqs. 21 and 22 into Eq. 6, we obtain the material response function in the NC approximation,

$$M(t_2, t_1) = \int d\Gamma_0 A(\Gamma(t_2); \Gamma_0) e^{-iU_{eg}(q_0)t_1} \rho_g(\Gamma_0; -\infty). \quad (23)$$

Here Γ_0 denotes the collection of initial conditions, $(\mathbf{p}_0, \mathbf{q}_0)$, for the phase points, and $A(\Gamma(t_2); \Gamma_0)$ is the target operator A written in terms of the phase space coordinates. As previously noted, once the material response function is

computed, it is straightforward to calculate both the optimal field and the spectroscopic response of the system in the weak response regime.¹³

The NC approximation has the advantage of leading to a tractable computational algorithm for systems of large dimensionality. As a confidence check, we apply this NC approximation to a gas phase I₂ system at room temperature and show the favorable comparison with both experimental and exact quantum results. In the next section, we will apply this approximation to a condensed phase system, I₂ in a cold Kr matrix, where no check with exact quantum mechanics is possible.

When we employ the NC approximation we must take care to preserve the causality of the system. Many time-frequency representations of the field do not satisfy this constraint, e.g., the Wigner and Husimi transformations. Yan has suggested the following causality transformation for the pump field,^{65,79}

$$I(w, t) = \frac{1}{\pi} \text{Re} \left[E^*(t) \int_0^\infty d\tau E(t - \tau) e^{-i\omega\tau} \right]. \quad (24)$$

Eq. 24 indicates that the field only contributes to the excitation for times previous to it, thereby preserving causality. In fact, this transformation follows naturally from Eq. 17 if we invoke the approximation given by Eq. 21. The excited state density matrix can be constructed as

$$\rho_e(\Gamma, t) = \int d\Gamma_0 \int_0^\infty dt' \mathcal{S}_{ee}(t - t') I(U_{eg}(\Gamma_0), t') \rho_g(\Gamma_0). \quad (25)$$

The NC theory presented here can capture the most important dynamical information of the system, and can therefore guide experimentalists in making optimal fields and predicting experimental outcomes. The comparison between exact quantum calculations and the NC theory has been carried out previously for a one dimensional system, and it was found that they agree well.¹⁵

After we irradiate the system with the optimal field, we need to be able to detect the outcome, in other words, we must have an experimentally realizable gauge that measures how well the control field has driven the system dynamics to the target state. The experimental detection technique we employ is Laser Induced Fluorescence (LIF). In a previous gas phase experiment,^{16,18} and in theoretical analyses,^{19,27} it has been demonstrated that the LIF signal contains the signature of wavepacket focusing, more specifically, at the target time, the observed LIF signal is localized when using the properly tailored ultrafast pump field. Thus, the sharpness or localization of LIF peaks indicate the focusing of the wavepacket at the probe window that is opened by a transform limited probe pulse. The LIF signals can be calculated quantum mechanically¹⁹ as well as using the NC approximation.

For a condensed phase system we are not able to obtain the exact wavefunction or density matrix, therefore it is computationally impractical to predict LIF signals with exact quantum mechanics. In general the transient probe absorption is recorded as a function of time delay, t_d , between

pump and probe pulses either as the total integrated signal, $S(t_d)$, or as a frequency-resolved transient signal, $S'(t_d, \omega)$, in which the transmitted probe field is further dispersed in the frequency domain. These two signals are defined by⁸⁰

$$S(t_d) = -2 \operatorname{Im} \int_{-\infty}^{\infty} dt E_T^*(t) P_T(t; t_d) = \int_{-\infty}^{\infty} d\omega S'(\omega, t_d) \quad (26)$$

and

$$S'(\omega, t_d) = 2 \operatorname{Im} [\tilde{E}_T^*(\omega) \tilde{P}_T(\omega, t_d)]. \quad (27)$$

Here $E_T(t)$ and $P_T(t, t_d)$ are the probe field and third order polarization functions, respectively, and $\tilde{E}_T(\omega)$ and $\tilde{P}_T(\omega, t_d)$ are their Fourier transforms. The key quantity for the calculation of the transient absorption is the third order polarization function.

We now apply the same NC approximation to the transition Green function between the $|e\rangle$ and $|f\rangle$ states, where $|e\rangle$ and $|f\rangle$ are the generic notation for the first and second excited states, respectively. In our gas phase experiment, these states correspond to the B and E states of I₂. We then obtain the NC transient absorption signal as,⁸¹

$$S(t_d) \approx \int_{-\infty}^{\infty} dt \operatorname{Tr} [|\mu_{fe}\rangle^2 I_T(U_{fe}, t) \rho_e(t + t_d)], \quad (28)$$

where $I_T(U_{fe}, t)$ is the causality transformation of the probe pulse defined as⁷⁹

$$I_T(\omega, t) = \frac{1}{\pi} \operatorname{Re} \left[E_T^*(t) \int_0^{\infty} dt' e^{i(\omega - \Omega_{fe})t'} E_T(t + t') \right], \quad (29)$$

where Ω_{fe} is the carrier frequency of the probe field. Within the classical approximation, we can write $\rho_e(t)$ as

$$\rho_e(t, R, R) = \frac{1}{N} \sum_i \delta[R - R_i(t)], \quad (30)$$

where Σ runs over all the phase space trajectories of the ensemble, $R_i(t)$ is the i th trajectory, and N is the total number of trajectories. Substituting Eq. 30 into Eq. 28, we get the final formula for calculating the LIF absorption using classical trajectories within the causality transformation,

$$S(t_d) \propto \sum_i \int_{-\infty}^{\infty} dt I_T(U_{fe}[R_i(t + t_d)], t). \quad (31)$$

Equation 31 is particularly simple and easy to implement computationally.

D. Numerical simulations for gas phase I₂

For the exact quantum simulation of the experimental LIF signals, there are two ways to choose the initial rovibrational eigenstates, $|v, J, M\rangle$. The first one is a straightforward, though tedious, direct summation over the initial rovibrational states, v and J (the energy does not depend on M), in Eq. 10 according to their Boltzmann weighting. For instance, setting $v=0 \rightarrow 9$ and $J=0 \rightarrow 150$, will involve a

TABLE I. Parameters for the I₂ Morse potential surfaces in the gas and condensed phases.^a

I-I	T _e (cm ⁻¹)	D _e (cm ⁻¹)	β(pm ⁻¹)	R _e (pm)
X	0	12550	0.019	267
B	15769	4381	0.018	302
E	41411	12536	0.016	365
f	43150	12536	0.017	364

^aReferences 19, 58, and 87.

very tedious averaging of 1510 initial rovibrational states. Further, each of these initial states will branch into two states (due to the selection rules) whose sum is non-stationary on the excited electronic state, and these two states will each spawn two states on the final probe potential energy surface. This is the main challenge to doing exact quantum rovibrational calculations for the pump-probe signal. The second alternative is to choose the initial rovibrational states using a Monte Carlo algorithm according to the thermal Boltzmann distribution. The energy of a rovibrational state is estimated from the following spectroscopic formula:⁸²

$$E_{v,J}^g = \hbar \left[\omega_e \left(v + \frac{1}{2} \right) - \omega_e x_e \left(v + \frac{1}{2} \right)^2 + B_v J(J+1) - D_v J^2(J+1)^2 + \omega_e y_e \left(v + \frac{1}{2} \right)^3 \right], \quad (32)$$

where

$$B_v = B_e - \alpha_e \left(v + \frac{1}{2} \right), \quad D_v = D_e + \beta_e \left(v + \frac{1}{2} \right), \quad D_e = \frac{4B_e^3}{\omega_e^2}, \quad (33)$$

and $\omega_e = 214.57$ cm⁻¹, $\omega_e x_e = 0.6127$ cm⁻¹, $\omega_e y_e = -0.000895$ cm⁻¹, $B_e = 0.03735$ cm⁻¹, $\alpha_e = 0.000117$ cm⁻¹, $\beta_e = 0$ are the spectroscopic constants.⁸² For a given temperature, we sample each v, J state according to its thermal weight,

$$W_{v,J} \propto \exp(-\beta E_{v,J}^g). \quad (34)$$

Note that each v, J state is $2J+1$ degenerate among different M states. Since we explicitly put the $2J+1$ in the summation (see Appendix), it is absent in Eq. 34. In our simulation, we choose 50 v, J states randomly by Monte Carlo sampling from the distribution defined by Eq. 34. The ranges of v and J considered are from 0 to 9 and 0 to 150, respectively. It turns out that averaging over 50 states obtained from such a sampling method gives converged results for the cases we are considering here. The radial part of each rovibrational eigenstate $u_v^g(R, t)$ is obtained using the Discrete Variable Representation (DVR) method,⁸³ and we use the split operator method to propagate the radial part of the wavefunction on a spatial grid.⁸⁴ The pump and probe electric fields are obtained from the experimental FROG data. In this calculation, the transition dipole is assumed to be coordinate independent, and the orientation is that of a parallel-parallel type transition. The parameters of the gas phase potential energy surfaces are listed in Table I. For the probe process, the

Franck approximation is used (see Appendix). The time step in the quantum propagation is 0.97 fs.

When the time delayed probe pulse is turned on, the angular distribution of the excited state molecules has changed from the initial $\cos^2 \theta$ distribution, due to the orientational effect of molecular rotation. For illustration, we can formulate this orientational decay as a function of delay time t for an ensemble of rigid diatomic rotors,

$$P(t) \propto \sum_{J=0}^{\infty} \exp\left[-\frac{\beta \hbar^2}{2I} J(J+1)\right] \left[\frac{2}{15} (2J+1) + \frac{1}{15(2J+1)} + \frac{4J(J+1)}{15(2J+1)} \cos(2J+1) \frac{\hbar t}{I} \right], \quad (35)$$

where I is the moment of inertia for the rigid rotor. The above equation also has a classical correspondence,

$$P(t) \propto \frac{16\pi^2 I}{5\beta} - \frac{32\pi^2 I t}{15\beta} \sqrt{\frac{2I}{\beta}} \exp\left(-\frac{2It^2}{\beta}\right) \int_0^{\sqrt{\frac{2I}{\beta}t}} dx e^{x^2}. \quad (36)$$

To check the accuracy of the NC theory, we apply it to the gas phase I₂ system. Although the quantum dynamics of this system can be calculated exactly, as described above, it is quite time consuming for a room temperature system. Therefore, the NC theory is also useful even for a simple gas phase thermal system. The simplicity of the NC calculation also makes it possible to directly include in the dynamics the spatial orientational effects, e.g. the temporal decay of the orientational distribution induced by the polarized light pulses, for either gas or condensed phase samples. This is different from the quantum calculations where the overlaps between spherical harmonics have to be evaluated explicitly.

The set of trajectories $\{R_i(0), \dot{R}_i(0)\}$ is sampled from the quantum corrected temperature Boltzmann distribution of velocities. The initial distribution of the I₂ vibrational coordinates is constructed from the causality transformation of the pump field and I₂ ground state potential. Applying Eq. 24, we obtain a time and coordinate dependent initial ensemble,

$$\rho_{I_2}(R, t) \propto e^{-\beta V_g(R)} |I[U_{eg}(R), t]|, \quad (37)$$

where R is the internuclear distance of the iodine molecule, V_g is the I₂ ground state potential, and U_{eg} is proportional to the difference between the ground and excited state potential energy surfaces of I₂, $U_{eg}(R) = (V_e(R) - V_g(R))/\hbar$. Note that the causality transformation is not positive definite (this is also true for the Wigner transformation), and therefore we have to label each initial phase space point according to its corresponding sign of the causality intensity $I[U_{eg}(R), t]$. The trajectories which have a negative weight will give a negative contribution to the material response function and to the final LIF signal. This feature is absent in usual MD simulations and arises from the quantum mechanical nature of the interference.

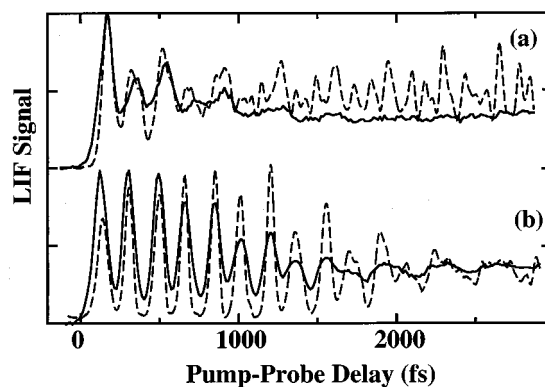


FIG. 5. Gas phase LIF signal as a function of delay between the pump and probe pulses calculated from quantum dynamics. The pump pulses used are those shown in Fig. 4 panels (b) and (d), and the probe pulse is as measured and described in the text. The solid lines are experimental results, the dashed lines are theoretical calculations. Panel (a) is the LIF signal from the positively chirped pump pulse (the pulse in panel b in Fig. 4), and panel (b) is the LIF signal from the negatively chirped pump pulse (the pulse in panel d in Fig. 4). As can be seen, theory without the thermal rotational distribution cannot well reproduce the experimental results. Experimental results have been normalized to the theory.

The momentum is chosen from a Boltzmann distribution at the artificial temperature⁷⁸ of 340 K (corresponding to the real experimental temperature of 313 K). The final signal is, in fact, insensitive to this temperature within small variations. This insensitivity to small variations in temperature was found to be true experimentally, as well. In each NC simulation, 4000 trajectories are used.

E. Simulation and experimental results: Gas phase

We now compare experimental and simulation results for gas phase control of I₂ vibrational motion. In Fig. 5, we show experimental results and simulated signals from quantum dynamics simulations which do not include rotational motion. The dashed line in panel 5(a) is the simulated LIF signal derived from the positively chirped pump pulse shown in panel (b) of Fig. 4, and the solid line is the experimental result. The dashed line in panel 5(b) is the simulated LIF signal from the negatively chirped pump pulse shown in panel (d) in Fig. 4, and the solid line is the experimental result.

From the experimental results considered alone, it is quite clear that the signal from the negatively chirped pump pulse is sharper and the oscillations last much longer than with the positively chirped pump pulse. This is because of the anharmonicity of the Morse potential. Higher vibrational states have longer vibrational periods, therefore, if the long time period (higher photon frequency) components of the I₂ vibrational wavepacket are initiated first and then followed by the excitation of the short period (lower photon frequency) components of the wavepacket, the components will eventually coalesce and focus before further dispersion.^{14,28,29} Therefore, the vibrational wavepacket initiated by a negatively chirped pump pulse can remain fo-

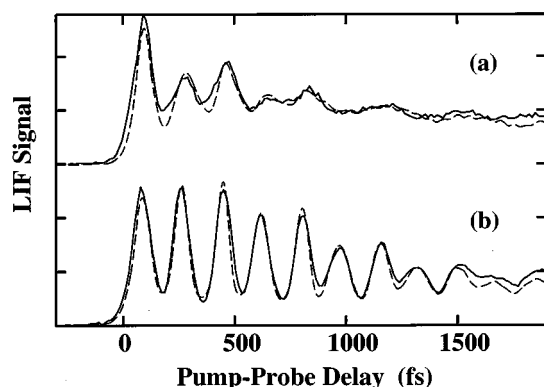


FIG. 6. Gas phase LIF signal as a function of delay between the pump and probe pulses calculated from exact quantum dynamics that include rotations, in particular the time evolution of the orientational distribution and the rotational-vibrational coupling due to the angular momentum dependent centrifugal potential. The pump and probe pulses are the same as those for Fig. 5. The solid lines are experimental results and the dashed lines are theoretical calculations. Panel (a) is the LIF signal from the positively chirped pump pulse and panel (b) is the LIF signal from the negatively chirped pump pulse. Experiments and theory are normalized to the same area.

cused for a longer time period than the vibrational wavepacket initiated by a positively chirped pump pulse. The positively chirped pump pulse, on the other hand, creates a wavepacket that disperses directly.

However, when we look at Fig. 5, which compares the theoretically calculated LIF signals with the experimental results, there is a substantial difference between them, because the rotational motion is not included in this calculation. Under the experimental conditions, $T=313$ K, many rovibrational states are thermally populated. The observed LIF signal decays also due to the decay of orientational localization arising from the dispersion in angular velocities in the thermal rotational distribution. It can be seen from Fig. 5 that the calculated signals match the experimental results reasonably well for the first ~ 600 fs, but diverge more and more at longer times. Although the thermal averaging over the initial population of vibrational states contributes to the delocalization of the LIF signal, the disagreement between simulation and experiment remains substantial if rotation is omitted from the calculations.^{10,11,75,76}

In Fig. 6, we show the comparison of gas phase I₂ experimental measurements (solid line) with exact quantum simulations (dashed line) which now include rotation, for the same positive and negative chirped pair of pump pulses as in Fig. 5. In this figure, the theoretical results are in excellent agreement with the experimental measurements, confirming the importance of rotational motion in wavepacket dynamics.^{10,11,75,76} More detailed analysis shows that there are two important rotational effects. The first is the decay of the anisotropic orientational distribution induced by the polarized pump pulse and then sampled by the polarized probe pulse. This effect can be experimentally eliminated by placing the pump and probe polarizations at the “magic angle.”⁷⁷ The second effect is due to the rotation-vibration

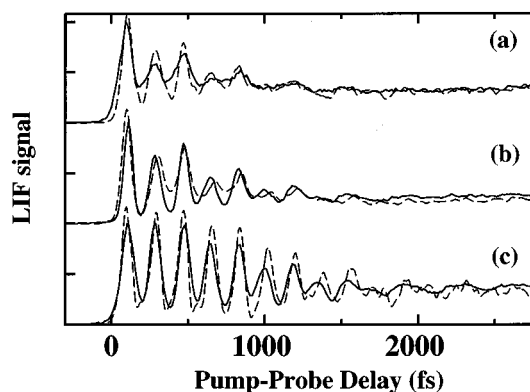


FIG. 7. Gas phase LIF signals as a function of delay between the pump and probe pulses calculated from Nearly Classical (NC) theory (dashed lines). The solid lines are experimental results. Panel (a) is the LIF signal from the positively chirped pump pulse (panel b of Fig. 4), panel (b) the LIF signal from the transform limited pump pulse (panel c of Fig. 4) and panel (c) the LIF signal from the negatively chirped pump pulse (panel d of Fig. 4). Experiments and theory are normalized to the same area.

multilevel structure, which can be eliminated by collapsing the rotational distribution by rotationally cooling the sample (e.g., in a molecular beam or cold matrix) or by projecting out a narrower distribution (e.g., by illuminating with a prepulse).

The overall rotational orientational decay is handled differently for the exact quantum calculations and the NC calculations. In the NC calculations, the ground state molecules are assumed originally to be isotropically oriented in space and, for a parallel transition, the excited state initially forms a $\cos^2 \theta$ distribution of internuclear axes about the polarization direction of the pump field due to the $\vec{D} \cdot \vec{E} = DE \cos \theta$ term in the rovibrational Hamiltonian, where we have chosen the electric field polarization to be along the Z-axis in the lab frame. When the time delayed probe pulse is turned on, the angular distribution of the excited state molecules has changed from the initial $\cos^2 \theta$ distribution, due to molecular rotation. This is an orientational effect, and is handled automatically (with no extra work) in the three dimensional NC approximation. For the exact quantum calculation, for numerical efficiency, the dynamics are one dimensional, and angular parts of the total wavefunctions are calculated analytically. Both the pure orientational effect and the spreading of the vibrational wavepacket due to the centrifugal coupling between vibration and rotation contribute. In Fig. 7, we show NC theory simulated and experimental LIF signals for positive, zero, and negatively chirped pump pulses. The dashed line signal in panel 7(a) is the simulated LIF signal that is derived from the positively chirped pump pulse shown in panel (b) of Fig. 4, and the solid line is the experimental result, and similarly for the transform limited (Figs. 7b and 4c) and negatively chirped (Figs. 7c and 4d) cases. Fig. 7 shows reasonably good agreement between experiment and simulation, the NC approximation reproducing the oscillations shown in the experimental LIF signals, and also capturing the trend of longer lasting localization of the wavepacket in the LIF signal for the negatively chirped pump

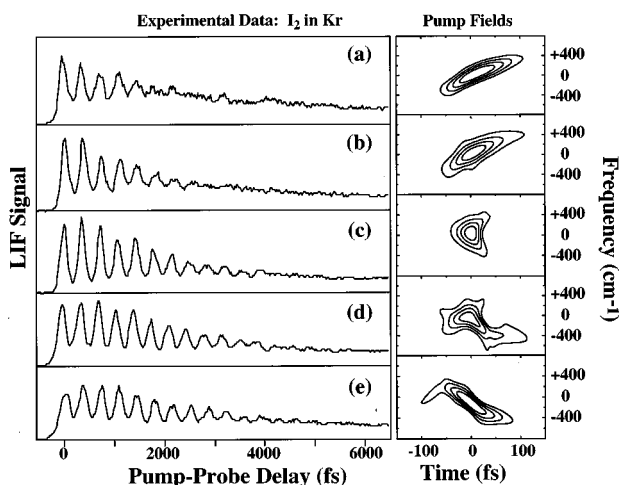


FIG. 8. Summary of the experimental results from the I₂ in solid Kr matrix at 15 K experiment. The left hand panel shows the collected LIF signals for excitation with pump pulses that have positive chirps (panels a and b), a transform limited pump pulse (panel c), and pump pulses that have negative chirps (panels d and e). The right hand panel shows the FROG-derived Wigner transforms of these pump fields. (An overall carrier frequency corresponding to 565 nm and a central time have been removed from the fields in presenting these figures.) The lowest contour levels of the Wigner representations, which are noisy, are not shown for reasons of clarity.

pulse over that of the matched positively chirped pump pulse.

From these NC simulations of gas phase I₂, we gain confidence in applying the approximate NC theory to more complicated condensed phase systems where the exact quantum simulations would be intractable. In the following section we describe the condensed phase experiments and apply the NC theory to simulate the condensed phase results and understand their meaning.

V. EXPERIMENTAL RESULTS: CONDENSED PHASE

We now present experimental results for the I₂/Kr 15 K condensed phase system. These experiments clearly demonstrate that the profound effect the tailoring of the pump pulse has on the vibrational dynamics of the I₂ molecule in the gas phase is also seen in the condensed phase. As in the gas phase, in order to clearly demonstrate this effect, we show that pairs of different pump pulses, each of which has nearly the same intensity vs. time, and intensity vs. frequency profiles, differing only in the time ordering of their frequencies, will lead to different vibrational dynamics of the I₂ molecules.

In Fig. 8 we summarize the results of the I₂/Kr experiments. The left hand panel shows the LIF signals for excitation with pump pulses that have positive chirps (panels a and b), transform limited pump pulse (panel c), and negative chirps (panels d and e). All of these pump pulses are experimentally arranged to have essentially the same frequency spectrum. The right hand panel of Fig. 8 shows the FROG-derived Wigner transforms of these pump fields. The probe pulse is a transform limited 50 fs pulse centered at 394 nm. This probe pulse opens a window at 360 pm on the B state

potential energy surface and every time the I₂ vibrational wavepacket crosses this window it will be further excited to the ion-pair state. Comparing Figs. 4 and 8, we find that there are about twice the number of peaks in the gas phase as in the condensed phase within the same time duration. This is because the probe window (see Fig. 1) is very near the turning point in the condensed phase, so that only one LIF peak is seen per vibrational period, and the probe window is between turning the points in the gas phase, so that two peaks per vibrational period are seen. The LIF signal that corresponds to excitation with a positively chirped pump pulse (panel b) clearly shows less structure and shallower modulation than the LIF signal that corresponds to excitation with a negatively chirped pump pulse (panel d). This means that the I₂ vibrational wavepacket initiated by the negatively chirped pump pulse retains its vibrational localization longer than the wavepacket initiated with the positively chirped pump pulse. The right hand panel of Fig. 8 demonstrates that the pump fields that give rise to the LIF signals in panels (b) and (d) are an approximately matched pair of chirped fields, although we found it considerably more difficult to make and measure the broader bandwidth pump pulses used in the condensed phase experiments in comparison to the narrower bandwidth gas phase pulses, and thus the matching is less exact. The LIF signals in panels (a) and (e) are also a result of an approximately matched pair of chirped pump fields. Again the LIF signal that is collected from the negatively chirped pump pulse (panel e) shows more structure than that of the LIF signal due to the positively chirped pump pulse (panel a). Thus, these results confirm that the control of vibrational dynamics by pulse tailoring is possible in the condensed phase, and that, as in the gas phase, for “reflectron” types of targets,^{14,27,29} negatively chirped pump pulses lead to a greater degree of wavepacket focusing and vibrational localization than positively chirped pump pulses. In contrast to the gas phase where, in the absence of collisions and population decay, the delocalization (and later relocalization) occurs with no loss of rovibrational coherence, in the condensed phase there is loss of coherence (T₂ processes) as well as loss of population (T₁ processes) involved in the dynamics. Thus relocalization due to the conservation of rovibrational phases will occur at later times in the gas phase, but will be damped out by dephasing processes in condensed phase systems.

In the next section we present the results of theoretical simulations of this experiment on the I₂/Kr system which show good agreement with experiment.

VI. THEORY: CONDENSED PHASE

A. Nearly classical control theory for the condensed phase

As we emphasized in the previous section, the NC method is particularly useful for large dimensional systems. In this section, we apply this method to a condensed phase system, I₂ in a cold Kr matrix. All the theory presented in Secs. IV C and D is applicable, except that now each phase

space trajectory evolves on a multidimensional potential energy surface. The I₂/Kr system Hamiltonian is

$$H = H_{I_2} + H_{Kr} + H_{int}, \quad (38)$$

where H_{I_2} is iodine molecular Hamiltonian and has same form as Eq. 4. H_{Kr} is the multidimensional krypton Hamiltonian and H_{int} is the interaction Hamiltonian between the iodine and krypton atoms. Quantum control has been formulated previously in terms of the reduced density matrix, defined as follows:^{22,23,46}

$$\rho_R(t) = \text{Tr}_{\text{bath}}[\rho(t)], \quad (39)$$

where Tr_{bath} means tracing over all the bath degrees of freedom in I₂/Kr system, the bath being defined here as the krypton atoms, the iodine molecular librations, and the iodine center of mass motion. The reduced density matrix describes the state and dynamics of the subsystem of interest, under the influence of its surrounding environment. Since the bath degrees of freedom have been traced out, the reduced density matrix only contains information pertaining to the I₂ internuclear vibrational motion. It is straightforward to combine the reduced density matrix approach with the NC approximation. In the NC picture, the density at each time is a set of Dirac delta functions, making the trace over the bath particularly simple. As a result, all the NC approximation equations presented for the gas phase in Secs. IV C and D generalize to the condensed phase, with the one extension that the I₂ vibrational trajectories now evolve under the influence of the Kr matrix.

B. Numerical simulations for the I₂/Kr system

To compute the classical dynamics the I₂/Kr system, we perform simulations in a repeating cubic unit cell of 108 Kr atoms. We replace the two adjacent Kr atoms at the center of the cell with two I atoms. In Fig. 9, we show the local structure with the iodine molecule and its first two Kr solvation shells. The interaction between any two Kr-Kr or I-Kr atoms is modeled with pairwise additive Lennard-Jones potentials, and the parameters for the interaction between iodine and krypton atoms are approximated by Xe-Kr potential parameters. These parameters are tabulated in Table II. The potentials for the I₂ electronic states are modeled by the following Morse potential,

$$V(R) = D_e(1 - e^{-\beta(R - R_e)})^2, \quad (40)$$

with the parameters given in Table I. The pump field excites I₂ to the electronic B state, the time delayed probe pulse then further excites the wavepacket to the ionic f state. The LIF signal from the ionic manifold is then detected as a function of delay time between the pump and the probe pulses.⁵⁷⁻⁵⁹

The initial configuration of the I₂/Kr system is obtained by using the artificial temperature method.⁷⁸ In this case, T in Eq. 19 (the real system temperature) is 15 K, and ω is chosen to be the Debye frequency of solid Kr, $\sim 60 \text{ cm}^{-1}$. Although this method is not exact for an anharmonic system, it should work well for this low temperature solid which is very harmonic in the ground equilibrium state. The artificial tempera-

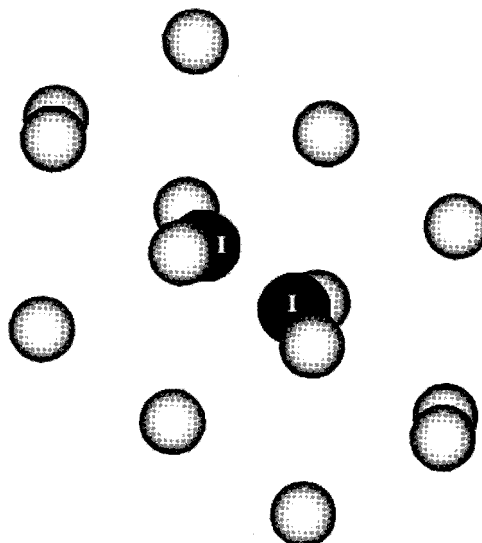


FIG. 9. Local structure of I₂ in a solid Krypton matrix, showing the first two shells around the I₂ molecule, with face centered cubic structure.

ture (T' in Eq. 19) is approximately 45 K. The initial distribution of the I₂ vibrational coordinate is obtained in a similar way as in the gas phase simulation. After we obtain the initial ensemble of I₂ internuclear distances, we sort them from smallest to largest values. Beginning with the smallest I₂ internuclear distance, we sequentially assign a distance to the iodine molecule in the face centered cubic crystal beginning with the smallest internuclear distance and equilibrate the Kr atoms at T' , holding the I₂ internuclear distance fixed. The face centered cubic crystal cell constant is 569 pm. The first equilibration is for 6 ps, and further equilibrations for new larger I₂ internuclear separations are for an additional picosecond. For each pump field, 2000 trajectories are run up to 5 ps, the time step being 1.94 fs. The time-coordinate initial ensemble contains all the information about the excitation process, therefore we can then monitor what happens during the excitation process. Once we have all the trajectories, the final LIF signal is obtained using Eq. 31.

We include the non-adiabatic population decay of population on the B state of I₂ due to the interaction with the condensed phase environment. This decrease in population is modeled as an overall exponential decay in the LIF signal as a function of time,

$$S^{\text{ad}}(t_d) = S(t_d)e^{-\gamma t_d}, \quad (41)$$

TABLE II. Parameters for the Lennard-Jones potential condensed phase surfaces.^a

	I-Kr	Kr-Kr
$\epsilon \text{ (cm}^{-1}\text{)}$	162.3	138.9
$\sigma \text{ (pm)}$	374	358

^aReference 58.

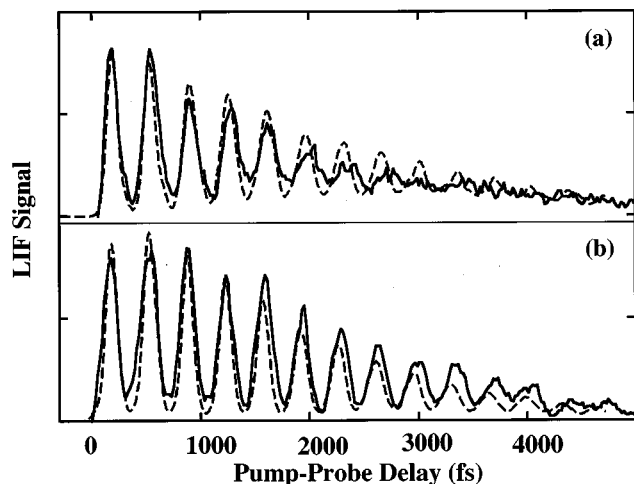


FIG. 10. Comparison of the simulation results for the I₂/Kr system with the experimental data. Panels (a) and (b), which correspond to panels (b) and (d) respectively of Fig. 8, show the comparison of the simulation results (dashed line) to the experimental results (solid line), for a positive and negatively chirped pump pulse, respectively. Experimental results are normalized to theory.

where $S(t_d)$ is the final LIF signal defined in Eq. 31, and γ is the overall decay constant which is chosen $\gamma = 0.13 \text{ ps}^{-1}$, in order to fit the condensed phase experimental data.

C. Simulation results: Condensed phase

In Fig. 10 we compare the results of the NC simulations to the experimental measurements obtained for the I₂/Kr condensed phase system. Panels (a) and (b) show the comparison of the simulation results (dashed line) to the experimental results (solid line) for positively and negatively chirped pump pulses, respectively. The pump and probe pulses used in the simulation are the experimentally measured pulses used in panels (b) and (d) respectively, of Fig. 8. As can be seen in Fig. 10, the simulation results agree reasonably well with the experimental data. The experimental trend of more vibrational localization in the LIF signal obtained from the negatively chirped pump pulse compared to the positively chirped pump pulse is captured by the simulation. In the following section we will discuss the ramifications of these results.

Another interesting experimental result is confirmed by the simulations. By comparing Figs. 8 (condensed phase) and 4 (gas phase), it is evident from experiment and theory that the observable vibrational localization persists longer in the condensed phase at 15 K than in the gas phase at 313 K. This result will also be discussed in the next section.

VII. DISCUSSION AND CONCLUSIONS

We have shown, both theoretically and experimentally, that a properly tailored light pulse can create a vibrational wavepacket that exhibits a long time persistence in its vibrational localization in both the gas and condensed phase. The observable localization persists *longer* in the condensed

phase than in the gas phase. The key to understanding this counter-intuitive result is the role of the initial ground electronic state distribution of rovibrational states in determining the observables. In the gas phase we prepare the system from a rovibrational distribution at 313 K. In the solid state (at 15 K), rotational and vibrational degrees of freedom are essentially frozen into their ground states, the cage allowing only small librations. In what follows we first discuss the gas phase results, with particular attention to the special role of rotations, and then discuss the condensed phase results, finally comparing and contrasting them.

The two main results to discuss concerning gas phase control of I₂ vibrational motion are the effect of the tailoring of the laser pulse on the vibrational dynamics, and the detrimental effects of the distribution of I₂ rotation as well as vibration on the vibrational localization of the wavepacket.

The effect of the linear chirp of the pump pulse on the vibrational localization has been discussed elsewhere,^{14,29} and we summarize those conclusions here. On the anharmonic B state potential, the higher energy components are more anharmonic, and have a longer period of oscillation than the lower energy components which are more harmonic and have a shorter oscillation period. To make these components of the wavepacket coalesce for times after the wavepacket reaches the outer turning point, the higher energy components must be excited before the lower energy components. A negatively chirped pump field will do just this. From this argument, it is easy to see why a negatively chirped pump pulse will create a wavepacket that evolves with a minimum of immediate delocalization, and a positively chirped pump pulse will create a vibrational wavepacket that delocalizes more directly. These qualitative arguments, which apply to both the gas phase and condensed phase examples, are developed more rigorously elsewhere.²⁹ Although the experimental data shows clearly that a negatively chirped pulse is much better than a positively chirped pulse at preserving the localization of the wavepacket, the comparison between a negatively chirped pulse and a transform limited pulse is less dramatic. The reason for this is that there are two factors at work when one chirps the pulse. By changing the frequency ordering, we can enhance or suppress the wavepacket spreading, but we also lengthen the pulse in time, which will result in a broader wavepacket, especially at early times. For negative chirps, these effects cancel each other, and whether we see dramatically sharper oscillations as we chirp the pulse depends on the interplay of pulse and molecular parameters. For positive chirps, these two effects work in concert, and the wavepacket delocalizes very quickly with chirp. Nevertheless, we emphasize that there is an absolute enhancement of the peak height in the gas phase with the negatively chirped pulse as opposed to the transform limited pulse. Thus chirping does result in a more focused wavepacket than does a transform limited pulse, albeit slightly, and in that sense it is an optimized light field.

The large effect of I₂ rotational dynamics on the observed LIF signals, particularly for longer times, is seen in the comparison of the theoretical simulations to the I₂ gas phase experimental data. Previous theoretical treatments of

wave packet interferometry experiments in gas phase I₂ (Refs. 75 and 76) have analyzed the effect of rotations in detail. The present 2 photon experiment is of a different nature than those experiments, however, and thus the role of rotations is different. The “inhomogeneous dephasing” of the oscillations seen in those experiments, which is analogous to a free induction decay of an electronic polarization, does not play a role in the present work, since the first pulse completes the one photon absorption and leaves the system in a population on the first excited state. The evolution of this population depends only on the excited state PES parameters, unlike the polarization in the interferometry experiments, which depends on the energy difference between the ground and excited state surfaces. Simple calculations also show that purely quantum effects, like the $J' = J'' \pm 1$ selection rule or nuclear spin degeneracy of the J'' states, do not play a role on the picosecond timescale that we observe the decay of the vibrational oscillations. The good agreement of the nearly classical and fully quantum calculations of the experimental LIF signal also provides evidence for the absence of purely quantum rotational effects. The orientational decay (which can be eliminated by magic angle pump-probe polarization⁷⁷), also plays a role but cannot explain the complete disappearance of the oscillations. By considering the excited state Hamiltonian,

$$h_e^J = -\frac{\hbar^2}{2\mu} \frac{\partial^2}{\partial R^2} + V_e(R) + \frac{J(J+1)\hbar^2}{2\mu R^2}, \quad (42)$$

we can think of each initial angular momentum of an I₂ molecule as contributing an effective potential energy term to the Hamiltonian. When added to the vibrational potential energy, this rotational term distorts the effective PES. Thus every angular momentum in the thermal distribution results in a different excited state PES on which the wavepacket propagates, and thus a different effective vibrational period. This distribution of effective vibrational frequencies, due to the initial distribution of angular momenta, results in a rapid decay of the observed oscillation due to destructive interference. For a heavy molecule like I₂ at high temperatures, this classical picture should be sufficient to understand the role of the rotations in contributing to the decay of the oscillations and the degradation of our ability to control the system. The negative effect of an initial distribution of rovibrational states on quantum control can be reduced either through cooling the sample by molecular beam expansion or by use of a cold matrix as we have done here, or through projecting out a narrower rovibrational distribution by excitation with a previous pulse or pulses. Such cooling by a cryogenic matrix is a major cause of the increased duration of vibrational localization in the condensed phase observed here.

Perhaps the most significant result of the present work is the clear demonstration of quantum control in the condensed phase. As in the gas phase, negatively chirped pump pulses produce a longer-lived vibrational localization. In contrast to the gas phase, the cold I₂/Kr matrix sample has little rovibrational excitation, and the I₂ molecule does not rotate but only librates in the Kr cage. The latter fact has been estab-

lished experimentally by noting that the fluorescence is fully polarized, and has been verified in the simulations.

The fact that the effect of the chirp on the vibrational localization is similar in both the gas and condensed phases simply indicates that the dynamics in this case is dominated by the I₂ (B) molecular potential, and only slightly perturbed by the lattice forces, which is also seen by examining the forces in the simulations. The observed decay of overall amplitude in the pump-probe signal is due to the decrease in vibrational population due to dissipation to the bath and to host induced electronic predissociation. With respect to the vibrational dynamics on the molecular B electronic state, these represent relatively small perturbations. Another significant difference between the gas and condensed phase environments is the fact that the decay of the absorption correlation function is much faster in the condensed phase than in the gas phase. For I₂ in Kr at 15 K, this time has been estimated to be on the order of 150 fs,⁸⁵ which is longer than the pulse durations used here. If the pulses were significantly longer than this time, we would expect to see some lessening of the control effect due to a broader initial wavepacket, although the present experiment is not nearly as sensitive as the above-mentioned interferometry experiments.⁸⁶ For a further discussion of the dissipative dynamics of I₂ in Kr, see the recent paper by Ovchinnikov *et al.*⁸⁵

Particularly at low temperature, it is clear that controllable localized vibrational evolution can persist in a condensed phase sample for many vibrational periods. By added a subsequent “locking” pulse, this localized distribution can be excited to another electronic surface leading to desired products and thus used to control the products of a chemical reaction by tailoring the pump (localization) pulse²⁵ as well as by varying the timing between pump and “locking” pulses.^{2,48} Thus the control of vibrational localization demonstrated here can be the basis of quantum control of chemical reactions in the condensed phase.

ACKNOWLEDGMENT

We thank Dr. Jianshu Cao for helpful discussions on rigid rotor LIF signals.

APPENDIX: FRANCK APPROXIMATION TO PROBE PROCESS IN QUANTUM CALCULATION

Treating the pump field as a first order time-dependent perturbation, the total wavefunction on the excited electronic state that is initiated from a ground J, M state, $\psi^e(R, \theta, \phi, t; J, M)$, can be written as

$$\psi^e(R, \theta, \phi, t; J, M) = \frac{u_{J-1, M}^e(R, t)}{R} Y_{J-1}^M(\theta, \phi) + \frac{u_{J+1, M}^e(R, t)}{R} Y_{J+1}^M(\theta, \phi), \quad (A1)$$

where $u_{J\pm 1, M}^e$ are defined in Eqs. 13 and 14. Note that if $J=0, M=0$, we will only have one term in above equation, the $J-1$ term being absent. Therefore, the total density matrix on the electronic excited state is

$$\rho^e(t) = \sum_{v,J=0}^{\infty} \sum_{M=-J}^J e^{-\beta E_{v,J}^e} |\psi^e(t;J,M)\rangle \langle \psi^e(t;J,M)|. \quad (\text{A2})$$

For simplicity, we do not write down the spherical coordinate representation explicitly in the above equation, but from now on, all the spatial variables will be in spherical coordinates unless otherwise specified. When we substitute Eq. A1 into Eq. A2, we get the density matrix in the coordinate representation. To calculate the asymptotic population on the final state after the probe pulse is over, we also apply first order perturbation theory to the probe process. We can then write down the wavefunction created from the ground J, M state on the final energy surface,

$$\psi^f(t;J,M) = -\frac{i}{\hbar} \int_{-\infty}^t dt_1 e^{-\frac{i}{\hbar} H^f(t-t_1)} \vec{D}_{fe} \cdot \vec{E}_2(t_1) \psi^e(t_1;J,M), \quad (\text{A3})$$

where $\vec{E}_2(t)$ is the probe light field, \vec{D}_{fe} is the transition dipole from the excited state to the final state, and H^f is the final state Hamiltonian. We choose the electric field polarization direction to be along the Z-axis in the space fixed frame. Therefore, for this parallel transition, $\vec{D}_{fe} \cdot \vec{E}_2 = D_{fe} E_2 \cos\theta$, and we have the wavefunction on the final state, $\psi^f(t;J,M)$, which is initiated from the ground J, M state as

$$\begin{aligned} \psi^f(t;J,M) \propto \frac{1}{R} \int_{-\infty}^t dt_1 D_{fe} E_2(t_1) & \left\{ \left[\frac{(J-M+1)(J+M+1)(J-M+2)(J+M+2)}{(2J+3)^2(2J+1)(2J+5)} \right]^{1/2} Y_{J+2}^M e^{-\frac{i}{\hbar} h_f^{J+2}(t-t_1)} u_{J+1}^e(R, t_1) \right. \\ & + \frac{(J-M+1)(J+M+1)}{(2J+3)(2J+1)} Y_J^M e^{-\frac{i}{\hbar} h_f^J(t-t_1)} u_{J+1}^e(R, t_1) + \frac{(J-M)(J+M)}{(2J-1)(2J+1)} Y_J^M e^{-\frac{i}{\hbar} h_f^J(t-t_1)} u_{J-1}^e(R, t_1) \\ & \left. + \left[\frac{(J-M)(J+M)(J-M-1)(J+M+1)}{(2J-1)^2(2J+1)(2J-3)} \right]^{1/2} Y_{J-2}^M e^{-\frac{i}{\hbar} h_f^{J-2}(t-t_1)} u_{J-1}^e(R, t_1) \right\}, \quad (\text{A4}) \end{aligned}$$

where h_f^J is the radial Hamiltonian for the nuclear motion on the electronic final state,

$$h_f^J = -\frac{\hbar^2}{2\mu} \frac{\partial^2}{\partial R^2} + V_f(R) + \frac{J(J+1)\hbar^2}{2\mu R^2}. \quad (\text{A5})$$

Due to the orthogonality of the spherical harmonic functions, the asymptotic population on the final electronic state can be calculated without involving these spherical harmonics explicitly in the computation. For simplicity, we denote the coefficients in the bracket in Eq. A4 as $C_1(J, M), C_2(J, M), C_3(J, M), C_4(J, M)$, respectively. Continuing the algebra, we then get the expression for the population on the final probe surface which is excited from the ground $|v, J, M\rangle$ state,

$$\begin{aligned} P(t;J,M) \propto \int_{-\infty}^t dt_1 \int_{-\infty}^t dt_2 |D_{fe}|^2 E_2(t_1) E_2^*(t_2) & [C_1^2(J, M) \langle e^{\frac{i}{\hbar} h_f^{J+2} t_2} u_{J+1}^e(R, t_2), e^{\frac{i}{\hbar} h_f^{J+2} t_1} u_{J+1}^e(R, t_1) \rangle + C_2^2(J, M) \\ & \times \langle e^{\frac{i}{\hbar} h_f^{J+2} t_2} u_{J+1}^e(R, t_2), e^{\frac{i}{\hbar} h_f^J t_1} u_{J+1}^e(R, t_1) \rangle + C_3^2(J, M) \langle e^{\frac{i}{\hbar} h_f^J t_2} u_{J-1}^e(R, t_2), e^{\frac{i}{\hbar} h_f^J t_1} u_{J-1}^e(R, t_1) \rangle + C_4^2(J, M) \\ & \times \langle e^{\frac{i}{\hbar} h_f^{J-2} t_2} u_{J-1}^e(R, t_2), e^{\frac{i}{\hbar} h_f^{J-2} t_1} u_{J-1}^e(R, t_1) \rangle + C_2(J, M) C_3(J, M) \langle e^{\frac{i}{\hbar} h_f^J t_2} u_{J+1}^e(R, t_2), e^{\frac{i}{\hbar} h_f^J t_1} u_{J-1}^e(R, t_1) \rangle \\ & + C_3(J, M) C_2(J, M) \langle e^{\frac{i}{\hbar} h_f^J t_2} u_{J-1}^e(R, t_2), e^{\frac{i}{\hbar} h_f^J t_1} u_{J+1}^e(R, t_1) \rangle]. \quad (\text{A6}) \end{aligned}$$

In the above equation, $\langle A(R, t_1), B(R, t_2) \rangle \equiv \int dR A^*(R, t) B(R, t)$. Note that the time t in the final state propagator has been canceled out due to the inner product. Physically, this is because we only calculate the final population, and the propagation on the final surface has no effect on this quantity. Since we only observe the total population after the probe pulse is over, we can replace the upper limit of the integral in Eq. A6 by ∞ , and therefore $P(t;J,M)$ is proportional to the experimental observable. The quantities in the inner products only depend on time t_1 and the time difference $t_2 - t_1$, so we can change the integration variable $t' = t_2 - t_1$, and the population as a function of delay, t_d , between the pump and probe pulses can be written as the following,

$$\begin{aligned} S_{v,J,M}(t_d) = 2\text{Re} \int_{-\infty}^{\infty} dt \int_0^{\infty} dt' E_2(t) E_2^*(t+t') & [C_1^2(J, M) \langle u_{J+1}^e(t+t'+t_d), e^{-\frac{i}{\hbar} h_f^{J+2} t'} u_{J+1}^e(t+t_d) \rangle + C_2^2(J, M) \\ & \times \langle u_{J+1}^e(t+t'+t_d), e^{-\frac{i}{\hbar} h_f^J t'} u_{J+1}^e(t+t_d) \rangle + C_3^2(J, M) \langle u_{J-1}^e(t+t'+t_d), e^{-\frac{i}{\hbar} h_f^J t'} u_{J-1}^e(t+t_d) \rangle + C_4^2(J, M) \\ & \times \langle u_{J-1}^e(t+t'+t_d), e^{-\frac{i}{\hbar} h_f^{J-2} t'} u_{J-1}^e(t+t_d) \rangle + C_2(J, M) C_3(J, M) \langle u_{J-1}^e(t+t'+t_d), e^{-\frac{i}{\hbar} h_f^J t'} u_{J+1}^e(t+t_d) \rangle \\ & + C_3(J, M) C_2(J, M) \langle u_{J+1}^e(t+t'+t_d), e^{-\frac{i}{\hbar} h_f^J t'} u_{J-1}^e(t+t_d) \rangle]. \quad (\text{A7}) \end{aligned}$$

Since $S_{v,J,M}(t_d)$ is only the contribution from a single ground $|v,J,M\rangle$ state, we need to sum over all the thermally populated ground states. It is not hard to see from the above equation that doing an exact propagation for each inner product is extremely tedious. It has previously been shown¹⁹ that the Franck approximation (vertical excitation) is good for short probe pulses. In our experiments, the probe pulses are of approximately 40-50 fs duration, and therefore this approximation will work reasonably well. The Franck approximation assumes that,

$$e^{-\frac{i}{\hbar}h_m t} e^{\frac{i}{\hbar}h_n t} \approx e^{\frac{i}{\hbar}h_n t} e^{-\frac{i}{\hbar}h_m t} \approx e^{-\frac{i}{\hbar}U_{mn} t}, \quad (\text{A8})$$

where $U_{mn} = h_m - h_n$. After we apply this approximation, the propagation on the final surface can be eliminated, and therefore the computation becomes much more efficient without losing much accuracy.

The total signal is obtained by summing over the individual signals from each $|v,J,M\rangle$ state,

$$S(t_d) = \sum_{v,J=0}^{\infty} \sum_{M=-J}^J \exp(-\beta E_{v,J}^g) S_{v,J,M}(t_d). \quad (\text{A9})$$

Since the ground $|v,J,M\rangle$ state energy is independent of magnetic quantum number, the sum over M can be done analytically.

$$\begin{aligned} \sum_{M=-J}^J C_1^2(J,M) &= \frac{2(J+1)(J+2)}{15(2J+3)}, \\ \sum_{M=-J}^J C_2^2(J,M) &= \frac{(J+1)[4(J+1)^2+1]}{15(2J+3)(2J+1)}, \\ \sum_{M=-J}^J C_3^2(J,M) &= \frac{J(4J^2+1)}{15(2J-1)(2J+1)}, \\ \sum_{M=-J}^J C_4^2(J,M) &= \frac{2J(J-1)}{15(2J-1)}, \\ \sum_{M=-J}^J C_2(J,M)C_3(J,M) &= \frac{2J(J+1)}{15(2J+1)}. \end{aligned} \quad (\text{A10})$$

Substituting Eq. A10 and Eq. A7 into Eq. A9, we then get the final LIF signal, including rotational and vibrational motion.

¹A. H. Zewail, *Phys. Today* **33**, 27 (1980).

²D. J. Tannor and S. A. Rice, *Adv. Chem. Phys.* **70**, 441 (1988).

³S. A. Rice, *Science* **258**, 412 (1992).

⁴M. Shapiro and P. Brumer, *J. Chem. Phys.* **84**, 4103 (1986).

⁵M. Shapiro and P. Brumer, *Int. Rev. Phys. Chem.* **13**, 187 (1994).

⁶B. Hartke, J. Manz, and J. Mathis, *Chem. Phys.* **139**, 123 (1989).

⁷A. M. Weiner, D. E. Leaird, G. P. Wiederrecht, and K. A. Nelson, *Science* **247**, 1317 (1990).

⁸H. Rabitz and S. Shi, *Adv. Mol. Vib. Coll. Dynam.* **1A**, 187 (1991).

⁹W. S. Warren, H. Rabitz, and M. Dahleh, *Science* **259**, 1581 (1993).

¹⁰V. Dubov and H. Rabitz, *J. Chem. Phys.* **103**, 8412 (1995).

¹¹L. Shen and H. Rabitz, *J. Chem. Phys.* **100**, 4811 (1994).

¹²B. Kohler, J. Krause, F. Raksi, K. R. Wilson, R. M. Whitnell, V. V. Yakovlev, and Y. J. Yan, *Acc. Chem. Res.* **28**, 133 (1995).

¹³Y. J. Yan, R. E. Gillilan, R. M. Whitnell, K. R. Wilson, and S. Mukamel, *J. Phys. Chem.* **97**, 2320 (1993).

¹⁴J. L. Krause, R. M. Whitnell, K. R. Wilson, Y. J. Yan, and S. Mukamel, *J. Chem. Phys.* **99**, 6562 (1993).

¹⁵J. L. Krause, R. M. Whitnell, K. R. Wilson, and Y. J. Yan, in *Ultrafast Reaction Dynamics and Solvent Effects*, edited by Y. Gauduel and P. Rossky (American Institute of Physics, New York, 1994), p. 3.

¹⁶B. Kohler, J. L. Krause, R. M. Whitnell, K. R. Wilson, V. V. Yakovlev, and Y. J. Yan, in *Ultrafast Phenomena IX*, edited by G. A. Mourou, A. H. Zewail, P. F. Barbara, and W. H. Knox (Springer, Berlin, 1994), p. 44.

¹⁷J. L. Krause, R. M. Whitnell, K. R. Wilson, and Y. J. Yan, in *Femtosecond Chemistry*, edited by J. Manz and L. Wöste (Springer, Weinheim, 1995), p. 743.

¹⁸B. Kohler, V. V. Yakovlev, J. Che, J. L. Krause, M. Messina, K. R. Wilson, N. Schwentner, R. M. Whitnell, and Y. J. Yan, *Phys. Rev. Lett.* **74**, 3360 (1995).

¹⁹J. Che, J. L. Krause, M. Messina, K. R. Wilson, and Y. J. Yan, *J. Phys. Chem.* **99**, 14 949 (1995).

²⁰M. Messina and K. R. Wilson, *Chem. Phys. Lett.* **241**, 502 (1995).

²¹J. L. Krause, M. Messina, K. R. Wilson, and Y. J. Yan, *J. Phys. Chem.* **99**, 13 736 (1995).

²²M. Messina, K. R. Wilson, and J. L. Krause, *J. Chem. Phys.* **104**, 173 (1996).

²³J. Che, M. Messina, K. R. Wilson, V. A. Apkarian, Z. Li, C. C. Martens, R. Zadoyan, and Y. J. Yan, *J. Phys. Chem.* **100**, 7873 (1996).

²⁴J. Che, M. Messina, K. R. Wilson, and Y. J. Yan, in *Femtochemistry, Ultrafast Chemical and Physical Processes in Molecular Systems*, edited by M. Chergui (World Scientific, Singapore, 1996), p. 360.

²⁵C. J. Bardeen, J. Che, K. R. Wilson, V. V. Yakovlev, P. Cong, B. Kohler, J. L. Krause, and M. Messina, *J. Phys. Chem.* (in press).

²⁶J. Cao and K. R. Wilson, *J. Chem. Phys.* **106**, 5206 (1997).

²⁷J. Cao and K. R. Wilson, *J. Chem. Phys.* **106**, 5239 (1997).

²⁸J. Cao and K. R. Wilson, *Phys. Rev. A* (in press).

²⁹J. Cao and K. R. Wilson (submitted).

³⁰C. Chen, Y. Y. Yin, and D. S. Elliott, *Phys. Rev. Lett.* **64**, 507 (1990).

³¹S. M. Park, S. P. Lu, and R. J. Gordon, *J. Chem. Phys.* **94**, 8622 (1991).

³²V. D. Kleiman, L. Zhu, J. Allen, and R. J. Gordon, *J. Chem. Phys.* **103**, 10 800 (1995).

³³V. D. Kleiman, L. Zhu, X. Li, and R. J. Gordon, *J. Chem. Phys.* **102**, 5863 (1995).

³⁴B. A. Baranova, A. N. Chudinov, and B. Y. Zel'dovich, *Opt. Commun.* **79**, 116 (1990).

³⁵N. F. Scherer, A. J. Ruggiero, M. Du, and G. R. Fleming, *J. Chem. Phys.* **93**, 856 (1990).

³⁶H. G. Muller, P. H. Bucksbaum, D. W. Schumacher, and A. Zavriyev, *J. Phys. B* **23**, 2761 (1990).

³⁷W. Jakubetz, J. Manz, and H.-J. Schreier, *Chem. Phys. Lett.* **165**, 100 (1990).

³⁸B. Just, J. Manz, and G. K. Paramanov, *Chem. Phys. Lett.* **193**, 429 (1992).

³⁹J. E. Combariza, B. Just, J. Manz, and G. K. Paramanov, *J. Phys. Chem.* **95**, 10 351 (1991).

⁴⁰J. S. Melinger, A. Hariharan, S. R. Gandhi, and W. S. Warren, *J. Chem. Phys.* **95**, 2210 (1991).

⁴¹J. S. Melinger, S. R. Gandhi, A. Hariharan, D. Goswami, and W. S. Warren, *J. Chem. Phys.* **101**, 6439 (1994).

⁴²K. J. Schafer and K. C. Kulander, *Phys. Rev. A* **45**, 8026 (1992).

⁴³B. Amstrup, J. D. Doll, R. A. Sauerbrey, G. Szabó, and A. Lőrincz, *Phys. Rev. A* **48**, 3830 (1993).

⁴⁴J. Janszky, P. Adam, A. V. Vinogradov, and T. Kobayashi, *Chem. Phys. Lett.* **213**, 368 (1993).

⁴⁵T. Baumert and G. Gerber, *Isr. J. Chem.* **34**, 103 (1994).

⁴⁶S. A. Rice and M. Zhao, in *Laser Techniques for State-Selected Chemistry II*, edited by J. W. Hepburn (SPIE, Bellingham, 1994), Vol. 2124, p. 246.

⁴⁷M. Sugawara and Y. Fujimura, *J. Chem. Phys.* **100**, 5646 (1994).

⁴⁸J. L. Herek, A. Materny, and A. H. Zewail, *Chem. Phys. Lett.* **228**, 15 (1994).

⁴⁹V. A. Apkarian, in *Femtochemistry, Ultrafast Chemical and Physical Processes in Molecular Systems*, edited by M. Chergui (World Scientific, Singapore, 1996), p. 603.

⁵⁰M. Sterling, R. Zadoyan, and V. A. Apkarian, *J. Chem. Phys.* **104**, 6497 (1996).

⁵¹V. A. Apkarian, C. J. Bardeen, J. Che, B. Kohler, C. C. Martens, M. Messina, K. R. Wilson, V. V. Yakovlev, and R. Zadoyan, in *Ultrafast*

- Phenomena X*, edited by J. Fujimoto, W. Zinth, P. F. Barbara, and W. H. Knox (Springer, Berlin, 1996), p. 219.
- ⁵²G. Q. Xing, X. B. Wang, X. Huang, and R. Bersohn, *J. Chem. Phys.* **104**, 826 (1996).
- ⁵³A. Assion, T. Baumert, V. Seyfried, and G. Gerber, in *Ultrafast Phenomena X*, edited by J. Fujimoto, W. Zinth, P. F. Barbara, and W. H. Knox (Springer, Berlin, 1996), p. 190.
- ⁵⁴Z. Chen, M. Shapiro, and P. Brumer, *J. Non. Opt. Phys. Mater.* **4**, 605 (1995).
- ⁵⁵A. Shnitman, I. Sofer, I. Golub, A. Yogeve, M. Shapiro, Z. Chen, and P. Brumer, *Phys. Rev. Lett.* **76**, 2886 (1996).
- ⁵⁶C. J. Bardeen, Q. Wang, and C. V. Shank, *Phys. Rev. Lett.* **75**, 3410 (1995).
- ⁵⁷R. Zadoyan, Z. Li, P. Ashjian, C. C. Martens, and V. A. Apkarian, *Chem. Phys. Lett.* **218**, 504 (1994).
- ⁵⁸R. Zadoyan, Z. Li, C. C. Martens, and V. A. Apkarian, *J. Chem. Phys.* **101**, 6648 (1994).
- ⁵⁹Z. Li, R. Zadoyan, V. A. Apkarian, and C. C. Martens, *J. Phys. Chem.* **99**, 7453 (1995).
- ⁶⁰E. D. Potter, Q. Liu, and A. H. Zewail, *Chem. Phys. Lett.* **200**, 605 (1992).
- ⁶¹Q. Liu, J.-K. Wang, and A. H. Zewail, *Nature* **364**, 427 (1993).
- ⁶²J. K. Wan, Q. Liu, and A. H. Zewail, *J. Phys. Chem.* **99**, 11 309 (1995).
- ⁶³S. Fei, X. Zheng, M. C. Heaven, and J. Tellinghuisen, *J. Chem. Phys.* **97**, 6057 (1992).
- ⁶⁴F. G. Amar and B. J. Berne, *J. Phys. Chem.* **88**, 6720 (1984).
- ⁶⁵R. M. Whitnell, K. R. Wilson, Y. J. Yan, and A. H. Zewail, *J. Mol. Liquid* **61**, 153 (1994).
- ⁶⁶J. P. Bergsma, M. H. Coladonato, P. M. Edelsten, J. D. Kahn, K. R. Wilson, and D. R. Fredkin, *J. Chem. Phys.* **84**, 6151 (1986).
- ⁶⁷V. S. Batista and D. F. Coker, *J. Chem. Phys.* **105**, 4033 (1996).
- ⁶⁸R. Zadoyan, M. Sterling, and V. A. Apkarian, *Faraday Trans.* **92**, 1821 (1996).
- ⁶⁹S. Mukamel, *The Principles of Nonlinear Optical Spectroscopy* (Oxford University, New York, 1995).
- ⁷⁰M. Gruebele, G. Roberts, M. Dantus, R. M. Bowman, and A. H. Zewail, *Chem. Phys. Lett.* **166**, 459 (1990).
- ⁷¹V. V. Yakovlev, B. Kohler, and K. R. Wilson, *Opt. Lett.* **19**, 2000 (1994).
- ⁷²K. R. Wilson and V. V. Yakovlev, *J. Opt. Soc. B.* **14**, 444 (1997).
- ⁷³R. Trebino and D. J. Kane, *J. Opt. Soc. Am. A* **10**, 1101 (1993).
- ⁷⁴B. Kohler, V. V. Yakovlev, K. R. Wilson, J. Squier, K. W. Delong, and R. Trebino, *Opt. Lett.* **20**, 483 (1995).
- ⁷⁵N. F. Scherer, A. Matro, L. D. Ziegler, M. Du, R. J. Carlson, J. A. Cina, and G. R. Fleming, *J. Chem. Phys.* **96**, 4180 (1992).
- ⁷⁶R. Bavli, V. Engel, and H. Metiu, *J. Chem. Phys.* **96**, 2600 (1992).
- ⁷⁷M. Dantus, R. M. Bowman, and A. H. Zewail, *Nature* **343**, 737 (1990).
- ⁷⁸J. P. Bergsma, P. H. Berens, K. R. Wilson, D. R. Fredkin, and E. J. Heller, *J. Phys. Chem.* **88**, 612 (1984).
- ⁷⁹Y. J. Yan, *Chem. Phys. Lett.* **198**, 43 (1992).
- ⁸⁰Y. J. Yan and S. Mukamel, *Phys. Rev. A* **41**, 6485 (1990).
- ⁸¹M. Lax, *J. Chem. Phys.* **20**, 1752 (1950).
- ⁸²G. Herzberg, *Molecular Spectra and Molecular Structure. I. Spectra of Diatomic Molecules*, 2nd ed. (Van Nostrand Reinhold, Princeton, 1950).
- ⁸³J. V. Lill, G. A. Parker, and J. C. Light, *Chem. Phys. Lett.* **89**, 483 (1982).
- ⁸⁴C. Leforestier, R. H. Bisseling, C. Cerjan, M. D. Feit, R. A. Friesner, A. Guldborg, A. Hammerich, G. Jolicard, W. Karrlein, H. Meyer, N. Lipkin, O. Roncero, and R. Kosloff, *J. Comput. Phys.* **94**, 59 (1991).
- ⁸⁵M. Ovchinnikov and V. A. Apkarian, *J. Chem. Phys.* **105**, 10 312 (1996).
- ⁸⁶N. F. Scherer, R. J. Carlson, A. Matro, M. Du, A. J. Ruggiero, V. Romero-Rochin, J. A. Cina, G. R. Fleming, and S. A. Rice, *J. Chem. Phys.* **95**, 1487 (1991).
- ⁸⁷J. C. D. Brand and A. R. Hoy, *Appl. Spectrosc. Rev.* **23**, 285 (1987).